Structural analysis and analogue modeling of the kinematics and dynamics of rockslide avalanches

Thomas Shea*
Benjamin van Wyk de Vries*
Laboratoire Magmas et Volcans, Université Blaise Pascal, Clermont-Ferrand, 63000, France

ABSTRACT

We present a structural analysis of subaerial natural and analogue rockslide avalanches. Such deposits often have well-developed faults, folds, and hummocks. These structures can be used to determine the kinematics and dynamics of emplacement. Large-scale terrestrial rockslide avalanches show large runout distances compared to their fall height. Most attempts to explain this phenomenon invoke fluidizing mechanisms or lubricating agents to reduce forces opposed to momentum, especially at the base. However, the properties and mechanics of low friction are still poorly understood. Any model for motion and emplacement must integrate geometric, morphologic, and structural features, all crucial in constraining kinematics and dynamics. Here we first examine the morphological and structural features displayed by 13 natural rockslide avalanche deposits; we then use simple and well-constrained analogue models involving the slide of stratified granular material down smooth, curved ramps. These differ from previous analogue models in that we concentrate on observing the structures produced by brittle deformation and use a low-friction sliding surface. Models show that variations in the sliding surface curvature, lateral profile, roughness, and modifications in material cohesion can successfully reproduce the majority of rockslide-avalanche deposit features. After discussing the geometrical and dynamic similarity between experiments and natural examples, we propose a model for structure formation and a fourfold classification based on model and natural deposit morphology and dynamics: hummocky, nonhummocky, dominantly extensional, and dominantly compressional rockslide avalanches. The models require a brittle core and surface that spreads and contracts by adjustment on large numbers of faults that bottom into a low-friction décollement layer. Spreading is accommodated by normal and strike-slip faults, while on deceleration, thrust faulting generates thickening. To be realistic, any physical predictive model must take into account these fundamental kinematic and structural aspects.

Keywords: rockslide-avalanche deposits, structures, faults, analogue modeling, avalanche transport, kinematics, hummocks.

INTRODUCTION

Rockslide Avalanches

Large-scale rockslide avalanches are part of the Earth mass-movement processes. Subaerial examples on Earth involve volumes of as much as 100 km^3, and their deposits cover areas as large as thousands of square kilometers, reaching distances >100 km (Stoopes and Sheridan, 1992). They cause considerable human and material loss, directly or through secondary events such as tsunamis, river obstruction, lahars, or magmatic eruptions (Siebert, 1984; Siebert et al., 1987). Although the onset of flank collapse was photographed at Mount St. Helens in the 1980 eruption (Voight, 1981), rockslide-avalanche formation and motion have never been clearly observed; as a result, study is mostly done through their deposits, or by theoretical modeling. Important gaps thus arise in understanding the emplacement kinematics and dynamics, because the link between deposit and emplacement is unclear.

Faults in Rockslide Avalanches

A striking feature of well-preserved rockslide-avalanche deposit surfaces is their morphology, which, through ridges and escarpments, shows the presence of a complex succession of faults and folds. One superb example of this is the Socompa rockslide avalanche (Central Andes, Chile and Argentina; Fig. 1), where the entire surface displays a dense network of normal, strike-slip, and thrust faults (Wadge et al., 1995; van Wyk de Vries et al., 2001, 2002; Kelfoun and Druitt, 2005; Kelfoun et al., 2008). The interior of this avalanche deposit, as seen in road cuts, shows that the fault structures incise deeply into the deposit interior (e.g., Fig. 3 in van Wyk de Vries et al., 2001; Figs. 1B, 1C herein). Other examples include the avalanches of Mombacho Volcano (Nicaragua; Shea et al., 2007), Parinacota (Clavero et al., 2002), and Flims (Pollet and Schneider, 2004). In each case, road cuts show either original material or granular rockslide-avalanche breccia layers being offset by numerous faults. Displacement is localized on narrow shear zones in the breccia, where the simple shear of the fault zone is accommodated. Such a structural pattern is common in faults in granular materials, seen in sandbox analogue models of volcano deformation (e.g., Merle and Borgia, 1996) or in natural breccia or pyroclastic successions deformed by slow tectonics (e.g., Borgia and van Wyk de Vries, 2003). These observations allow us to characterize the structures observed here as faults, as this is the closest and most suitable broad definition available. The data indicate that large-scale brittle

*Shea, corresponding author: present address: Geology and Geophysics Department, SOEST, University of Hawaii at Manoa, Honolulu, USA; tshea@hawaii.edu. van Wyk de Vries: b.vanwyk@opgc.univ-bpclermont.fr.

Geosphere; August 2008; v. 4; no. 4; p. 657–686; doi: 10.1130/GES00131.1; 15 figures; 2 tables; 2 supplemental tables; 1 supplemental file; 2 animations.

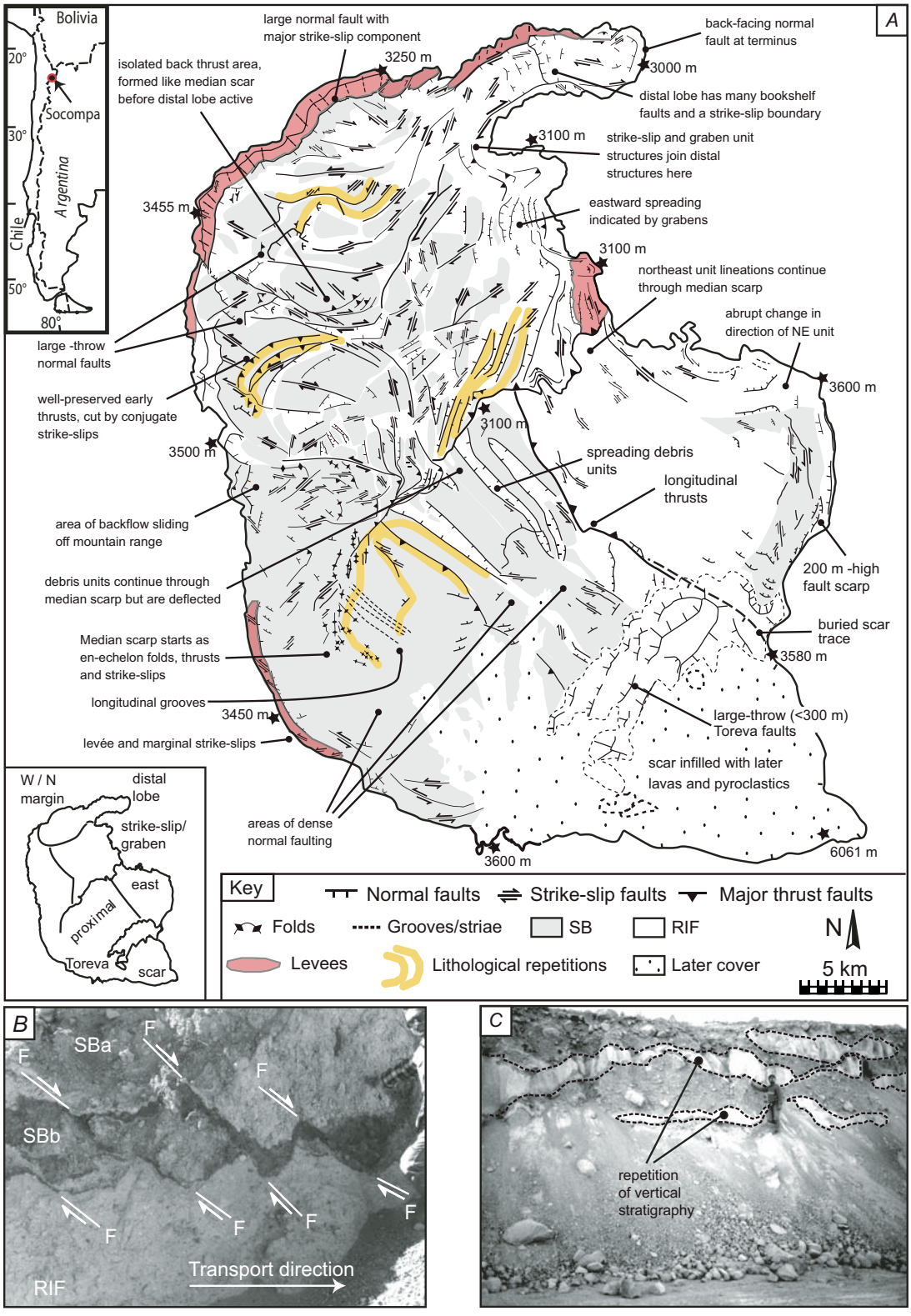

Figure 1 (*continued on next page*). **(A) Volcán Socompa (Central Andes, Chile and Argentina) rockslide-avalanche deposit structural map with main features (Guilbaud, 2000; van Wyk de Vries et al., 2002). The map is made from detailed aerial photographs, a digital elevation model (DEM), and field observations. Only the main structures are shown. (B) Outcrop photograph of normal faults developed in breccia at Socompa (from van Wyk de Vries et al., 2001). These are proximal normal faults that are deformed by latter strike-slip faults as shown in Figure 2A. (C) Vertical lithological repetitions (man for scale) at a marginal site shown in vertical cut, normal to transport direction of the dense banding seen in F. The repetition is similar to that seen in the analogue models. The white (basal) layers are Reconstituted ignimbrite facies (RIF; dominantly fine materials from the remobilized ignimbritic substratum), and the gray (upper) is the Socompa Breccia (SB; blocks + matrix) (van Wyk de Vries et al., 2001).**

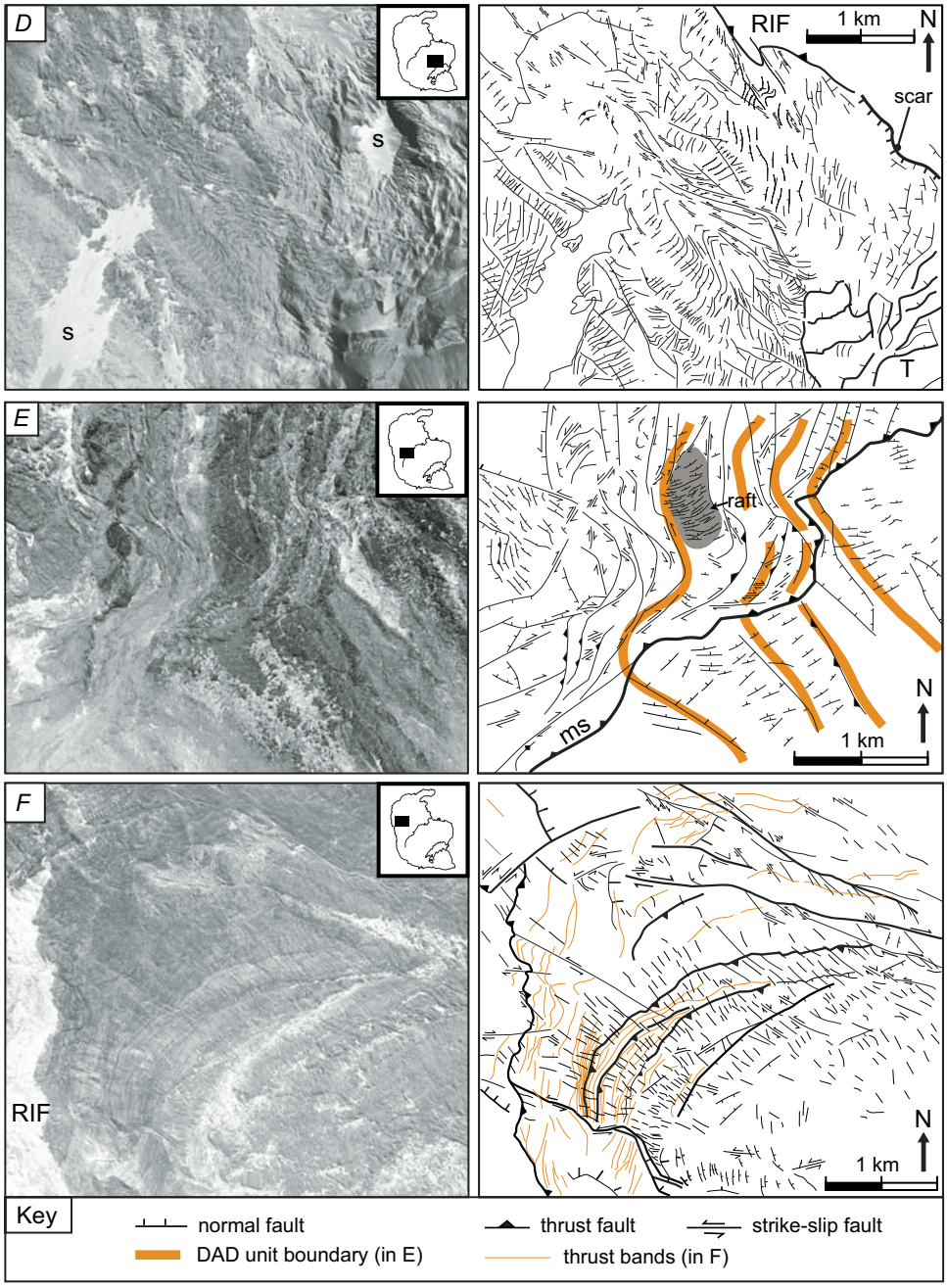

Figure 1 (*continued*). Three detailed structural maps of the Socompa deposit, made from aerial photographs after field inspection (van Wyk de Vries et al., 2001, 2002). Structures are shown at a greater resolution. Note that there are numerous crosscutting relationships between faults that indicate multiple generations of fault structures. Some crosscutting relationships have displacements too small to show on the map, others have displacements of several kilometers. (D) Proximal zone including the Toreva block margin (T) and edge of collapse scar (scar). Here Toreva blocks have 10–100-m-spaced large normal faults that become denser in the direction of transport. (The Torevas transform over a short zone of ~500 m to a fully brecciated rockslide avalanche.) Normal faults (illustrated in B) are displaced and deformed by later strike-slip faults and broad zones of shear that at small scale, are made up of many smaller discrete fault planes. S indicates small salar deposits on the deposit surface. (E) Central zone of deposit cut by the major Median Scarp (ms) thrust belt (Guilbaud, 2000; Kelfoun et al., 2008). Note that the proximal structures to the southeast are cut and the deposit banding is deflected across the median scarp. Note also that islands or rafts of normally faulted blocks are preserved in the predominantly strike-slip deformed zone to the northwest of the median scarp (raft). (F) Distal area with fine-scale banding, cut by thrusts and strike-slip faults. Note that the outer margin of the deposit is composed of the RIF basal facies. The banding is interpreted to originate from the multiple thrusting of lower RIF facies and upper SB facies (van Wyk de Vries et al., 2001, 2002; Kelfoun et al., 2008). Note the large displacement strike-slip faults to the northeast, and the dense late-formed strike-slip faults: some of these clearly displace the earlier thrust faults, while on some lineaments no offset can be seen. The thrusts may have originated initially as normal faults that were subsequently rotated and inverted into thrusts during the deceleration phase. In this area the slide was riding up a topographic slope and there is also major late-stage sliding in the reverse direction (Kelfoun et al., 2008), with a second set of structures produced. DAD—Debris Avalanche Deposits.

deformation occurs in the main mass during rockslide-avalanche emplacement.

Rockslide-Avalanche Kinematics

Socompa and other deposits like Blackhawk (Fig. 2A), Chaos Jumbles (Fig. 2B), or Mombacho (Fig. 2C) are morphologically and geometrically very different from each other. Various combinations of undulations, hummocks, ridges, and troughs cover their surfaces, and their respective outlines differ significantly. Any kinematic or dynamic model for rockslide-avalanche emplacement should account for all these morphological and structural features, as indicated in Pudasaini and Hutter (2007), or Cruden and Varnes (1996). However, few studies (e.g., Belousov et al., 1999; Clavero et al., 2002; van Wyk de Vries et al., 2002; Kelfoun and Druitt, 2005) have focused on these aspects, even though they are crucial in defining basic constraints. For example, if the original pre-collapse gross stratigraphy is preserved within a deposit, turbulent transport models involving significant large-scale mixing are not feasible. Similarly, if surface faults form throughout emplacement, a brittle-type behavior must be accounted for in physical models. In turn, the depth reached by these faults may provide information on the transition between a brittle

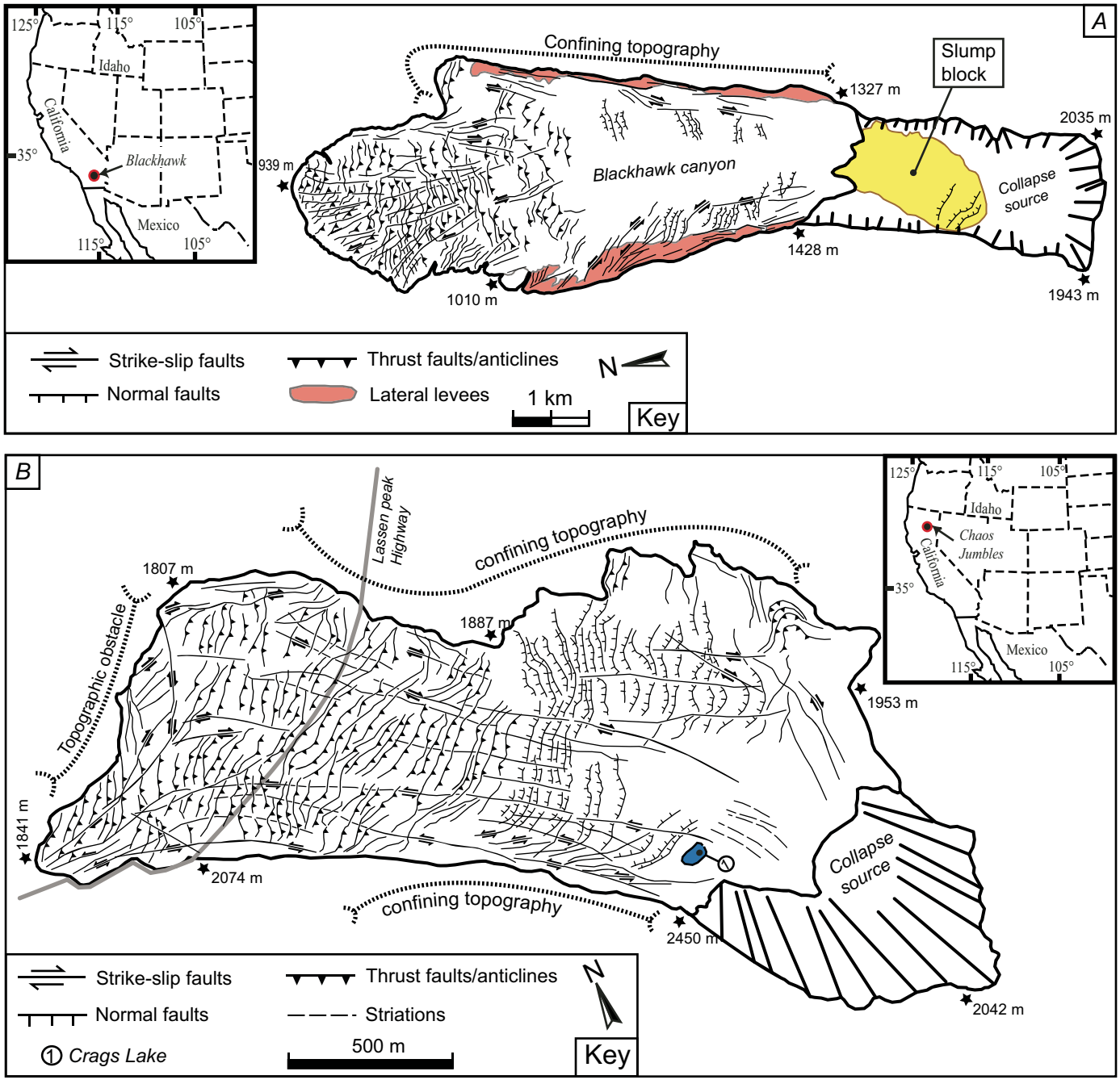

Figure 2 (*continued on next page*). Structural maps. (A) Non-volcanic rockslide avalanche, Blackhawk (California, USA). (B) Volcanic rockslide avalanches: Chaos Jumbles (California, USA).

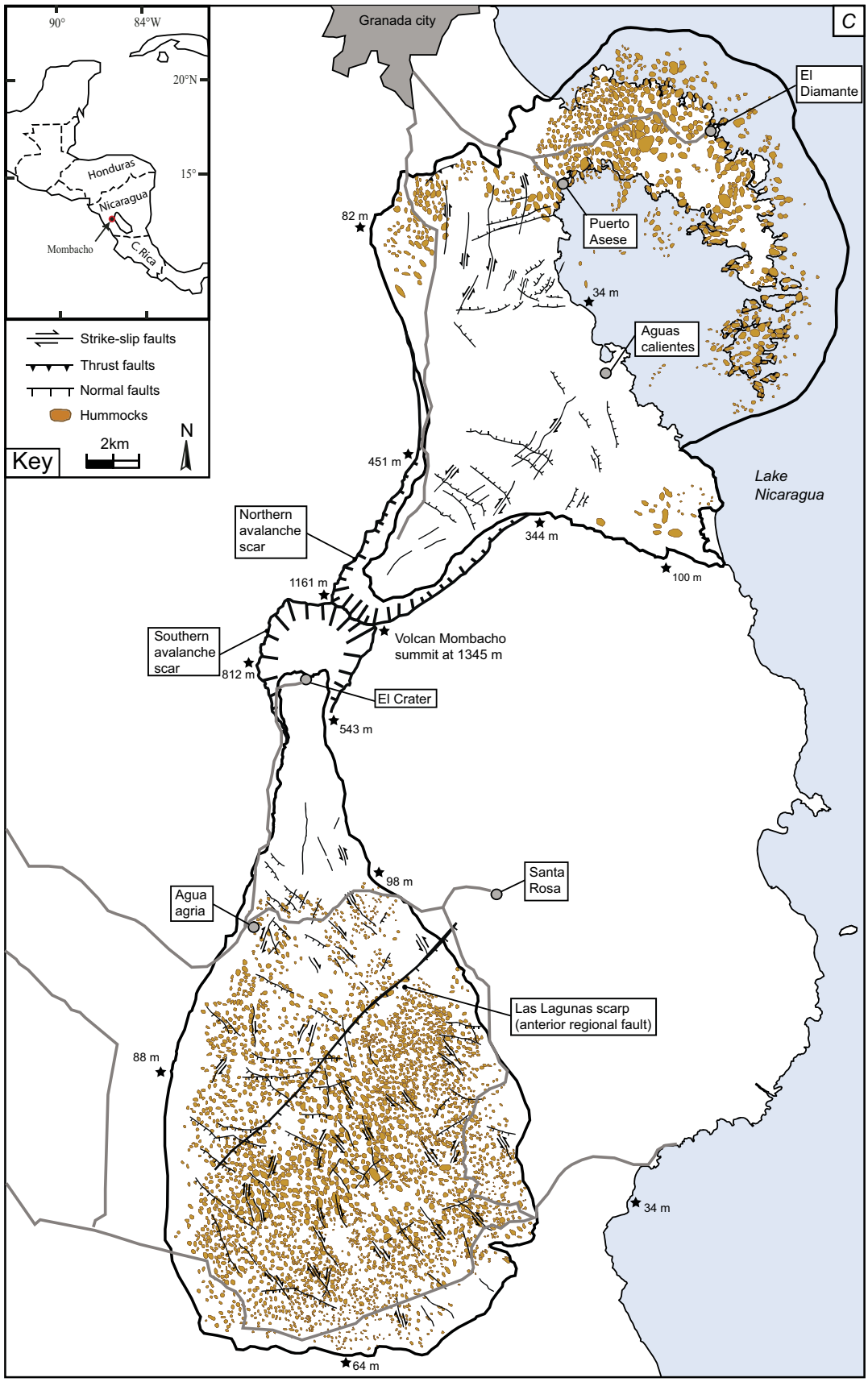

Figure 2 (*continued*). (C) Mombacho North and South (Nicaragua). Note the differences in surface structure organization where Blackhawk and Chaos Jumbles have ridged and fault-rich surfaces, contrary to those from Mombacho North and South, both ridge poor and hummock rich.

crust and a basal liquefied and/or fluidized low-friction slide layer.

Remote Sensing Analysis and Modeling

Through detailed remote sensing analysis and analogue modeling of rockslide-avalanche deposit geometry, internal structures, and surface morphology, our approach constrains rockslide-avalanche kinematics and allows us to make predictions about their emplacement dynamics. Remote sensing is generally used because deposits are large and often inaccessible. However, the surface morphology records clearly the structures that are developed within the deposit, allowing structural maps to be created. Field verification has been made on Socompa and Mombacho deposits (van Wyk de Vries et al., 2001; Shea et al., 2007), and provides the ground truth for the structures. Other deposits also have field descriptions of faulting, such as Mount St. Helens (Glicken, 1998), Parinacota and Ollagüe (Clavero et al., 2002, 2005), and those described by Shaller (1991).

This paper also presents a series of analogue experiments that reproduces the slide of a stratified mass of sand with variable cohesion down a simple curved ramp. Resulting experiments were photographed, filmed, studied in cross section, and characterized both quantitatively and qualitatively. The models are scaled and we compare results to natural examples. The models deform in the frictional granular regime, the deformation is ruled by brittle mechanics, and faulting is generated as in the natural examples. We show that this approach can be used effectively in the interpretation of structures in the field.

ROCKSLIDE AVALANCHES: PROBLEMS

On Earth, large mass movements occur in four major environments: on submarine volcanoes, on continental slopes, on continental volcanoes, and on mountain chains. This study focuses on subaerial collapses, although submarine ones may behave in a similar fashion, as the deposit morphology is similar (e.g., Oehler et al., 2004). The basic phenomenon involves failure and collapse of a rock mass that accelerates until it reaches a slope sufficiently low or long to be brought to a stop. The term "debris avalanche" has been used rather loosely, hence the need to define it more precisely. We chose the term rockslide avalanche, as it best describes the brittle and fluidized nature of the phenomena. To a first approximation we use the definition of Crandell (1989, p. 1), who described rockslide avalanches as "rapidly moving unsorted mixtures of blocks and matrix, mobilized by gravity consequently to [volcano] flank destabilizations." This definition is general enough to include non-volcanic rockslide avalanches. When the rock mass collapses, it transforms into a moving rockslide avalanche due to fragmentation processes or an initially fragmented state (Voight et al., 1983; Glicken 1991), and travels over the landscape at speeds up to 300 km/h, while thinning and spreading. When the mass loses sufficient kinetic energy, it comes to rest, depositing material tens of meters in thickness over distances often greater than 10 km. Rockslide-avalanche deposits frequently expose a bimodal lithology, described by Ui (1983) and Glicken (1991) as block facies and mixed facies (matrix and blocks). Often, the block facies forms the upper section of the deposit and covers the mixed facies (Crandell, 1989; Shaller, 1991; Belousov et al., 1999; Clavero et al., 2002, 2005; Reubi and Hernández, 2000; Shea et al., 2007); consequently, a gross inverse grading may exist, which opposes the use of the term "unsorted" in the definition of Crandell (1989). In contrast to debris flows or mudflows, rockslide avalanches comprise a significantly lower proportion of fluids, and are therefore said to be unsaturated.

Rockslide-Avalanche Mobility

Studies on rockslide-avalanche dynamics have generally focused on their long runout. In general, runout is related to a friction coefficient, defined as the tangent to the slope connecting the pre-collapse and post-collapse centers of gravity of the rock mass (Fig. 3A). Preexisting topography being difficult to evaluate, Heim (1932) proposed to approximate this coefficient to the tangent of the slope joining the scar high point to the furthest point reached by the rockslide avalanche: he named this "fahrböschung," generally referred to as "apparent friction coefficient," and calculated dividing fall height *H* by the horizontal runout *L*. Scheidegger (1973) noticed that a direct relationship exists between non-volcanic rockslide-avalanche volumes *V* and their apparent friction coefficients: *H*/*L* decreases systematically with volume increase. Ui (1983) reached similar conclusions regarding volcanic mass movements. With the available data, he further suggested that volcanic *H*/*L* ratios were smaller than non-volcanic ratios at similar volumes. McEwen (1989) compared terrestrial rockslide-avalanche volumes

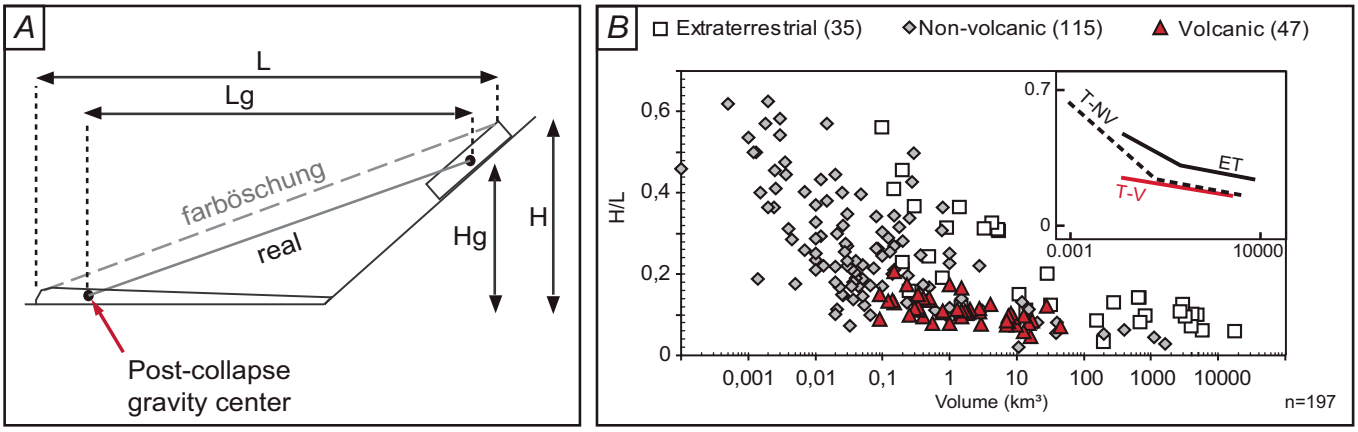

Figure 3. (A) Comparison of apparent friction coefficient (farböschung) with real friction coefficient. *H* and *L* measure height and length using the uppermost point of the collapse scar and the distant tip of the deposit, whereas H_g and L_g relate to the original and final gravity centers of the involved rock mass. (B) Plot of *H*/*L* versus volume for the gathered rockslide-avalanche data from different environments. Volume is in log scale and n is the number of data points. Subplot displays fitted trends for all three environments, where ET = extraterrestrial, T-NV = terrestrial non-volcanic, and T-V = terrestrial volcanic.

and *H*/*L* ratios with their Martian equivalents, and discovered that on average, Martian *H*/*L* ratios are lower than terrestrial *H*/*L* ratios for similar volumes. He suggested that such variations arise from gravity differences, as Martian events need a much thicker flow to reach identical runout.

In order to verify the validity of such observations, we gathered an up-to-date database (sources: Howard, 1973; Lucchitta, 1979; Francis et al., 1985; Siebert et al., 1987; McEwen, 1989; Shaller, 1991; Schenk and Bulmer, 1998; Clavero et al., 2002; Shea et al., 2007) and compiled measurements for 35 extraterrestrial (Moon and Mars), 47 terrestrial volcanic, and 115 terrestrial non-volcanic rockslide avalanches. Figure 3B plots *H*/*L* versus *V* data for each separate environment and gathers them into a single graph for comparison. Regression lines ($H/L \approx 0.25V^{-0.13}$ for extraterrestrial and for $H/L \approx 0.14V^{-0.16}$ terrestrial) have too much scatter for further quantitative use ($0.36 < R^2 < 0.63$), but nonetheless show general trends. Note that in such a large database, some of this scatter may be attributed to differences in volume and runout calculation, as well as measurement techniques. As suggested by Legros (2002), we also plotted *L* versus *V* (i.e., disregarding *H*) and, while R^2 values obtained are somewhat better (less scatter), the relative positions of trends were similar to when *H* was included.

Overall, terrestrial and extraterrestrial trends show similar general behavior. However, extraterrestrial data are systematically shifted toward smaller *H*/*L* ratios at similar volumes. This confirms previous observations made by McEwen (1989). In all cases, the data also confirm the volume effect described by Scheidegger (1973) and Ui (1983), although above certain volumes (~1 km^3 for terrestrial and ~10 km^3 for extraterrestrial), *H*/*L* decreases more smoothly.

Contrary to hypotheses made by Ui (1983), volcanic *H*/*L* ratios are not significantly lower than non-volcanic *H*/*L* at a given volume. However, comparing the two environments is not entirely conclusive because 73% of the non-volcanic data we currently have is restricted to volumes <0.1 km^3, whereas 95% of the volcanic data available are >0.1 km^3. Possibly, the lack of data for volcanic mass movements of $V < 0.1$ km^3 relates to their frequent transformation into lahars. In conclusion, the comparison between terrestrial volcanic and non-volcanic data is only able to demonstrate that volcanic rockslide avalanches reach higher volumes more frequently than non-volcanic events. Other than this, no significant difference in terrestrial volcanic and non-volcanic behavior can be distinguished, which slightly diverges from the conclusions of Ui (1983), but is in agreement with those of Shaller (1991). The conclusion is important because it means that volcanic and non-volcanic events can essentially be treated as one phenomenon.

GEOMETRICAL, STRUCTURAL, AND MORPHOLOGICAL CHARACTERISTICS OF ROCKSLIDE-AVALANCHE DEPOSITS

We characterized a total of 13 terrestrial and 1 extraterrestrial rockslide avalanches in terms of structural, geometrical, and morphological features (Table 1; Figs. 1, 2, 4, and 5; see also Supplemental File[1]) prior to the experimental work. Their structural maps were built using a combination of available imagery, digital elevation models, available literature (Shreve, 1968; Eppler et al., 1987; Francis and Wells, 1988; Shaller, 1991; Wadge et al., 1995; Guilbaud, 2000; van Wyk de Vries et al., 2001, 2002; Clavero et al., 2002, 2005; Shea et al., 2007), and field observations. The general guidelines we used to choose these deposits were a function of the following:

1. The presence of structures on their surface (no significant erosion or reworking);
2. The quality and/or resolution of photographic and/or remote sensing data available;
3. Their runout (generally $H/L \leq 0.3$);
4. The environment (at least one for each terrestrial volcanic, terrestrial non-volcanic, and extraterrestrial);
5. The range of volumes they cover (0.026–40 km^3 for terrestrial deposits and one extraterrestrial >500,000 km^3);
6. The absence of associated volcanic eruption;
7. The state of preservation of the deposit (e.g., no significant erosion, reworking of material, or eruptive material cover);
8. Their diverse but relatively well constrained and fairly simple topography-deposit relationship;
9. Their profiles (at least one of each uniform, distally raised, proximally raised);
10. Both hummock-rich and hummock-free cases need to be represented; and
11. The quantity of data available from previous studies.

For example, Mount St. Helens, Shiveluch, Ontake-San, and Bezymianny rockslide avalanches were discarded, given that their emplacement was associated with intense eruptive activity, which can potentially mask important structures. In the well-documented case of Mount St. Helens, the very complex topographic setting, the reworking of materials by erosion, and the pyroclastic and lahar cover prevent clear surface structure observation.

Plan-View Shape

Deposits created by large-scale collapses may partly or fully adopt four distinct shapes: (1) fan shaped (e.g., Ollagüe, Fig. 4E; Tetivicha, Fig. 5A; Llullaillaco "northern subunit," Fig. 5B) with linear proximal and/or distal margins and variably lobate distal margins; (2) single lobes (e.g., Carlson, Fig. 4A; Martinez Mountain, Fig. 4B; Blackhawk, Fig. 2A; Mombacho North and South, Fig. 2C; Socompa, Fig. 1; Olympus Mons, Fig. 5D) with well-curved lateral and distal margins; (3) tongue shaped (e.g., Aucanquilcha, Fig. 4C; Llullaillaco, Fig. 5B; Socompa "East subunit," Fig. 1) with parallel lateral margins and a curved distal margin; and (4) irregular: i.e., heterogeneous depositional topography such as valleys or topographic highs and/or barriers often prevent rockslide-avalanche deposits from adopting fan-shaped, single lobe, or tongue-shaped outlines (e.g., Chaos Jumbles, Fig. 2B; Parinacota, Fig. 5C).

Profiles

In cross section the profiles may appear as dominantly: (1) uniform (e.g., Aucanquilcha, Chaos Jumbles, Lastarria, Mombacho South, Llullaillaco, Socompa East, and perhaps Olympus Mons) with constant thickness throughout the deposit; (2) distally raised (e.g., Carlson, Blackhawk, Mombacho North, Ollagüe, Socompa West), where the frontal margin is thicker than the proximal; (3) proximally raised (e.g., Parinacota) with thickness decreasing with distance; (4) irregular (e.g., Tetivicha, Martínez Mountain), where thickness varies significantly, unrelated to distance from the source.

Constituent Textures

The brecciated state of the materials enclosed in the deposit is probably the most common internal characteristic of a deposit. In addition, the deposits always show a cohesive travel mode; for example, roads or houses located a few meters from the margins (the latter may measure several hundreds of meters in height)

[1]If you are viewing the PDF of this paper or reading it offline, please visit http://dx.doi.org/10.1130/GES00131.SF1 (Supplemental File 1) or the full-text article on www.gsajournals.org to view Supplemental File 1, a Google Earth (.kml) placemark file containing the locations of the investigated rockslide avalanches. To view the file, you will need Google Earth, which can be downloaded at http://earth.google.com.

TABLE 1. ROCKSLIDE-AVALANCHE INFORMATION AND STRUCTURAL CHARACTERISTICS

Environment	Name (Country)	Figure	Volume (km^3)	Shape	Profile	Confinement	Preserved stratigraphy	Gross inverse grading	Substratum incorporation	Jigsaw breccia	Hackly textures	Clast orientation	Collapse amphitheater striae	Lithological repetitions	Thrusts	Normal faults	Strike-slip faults	Hummocks	Torevas	Longitudinal ridges	Transverse ridges	Traverse arched ridges	Lateral levees
T	Carlson (USA)	4A	0.1	L	DR	C	M	O	O	–	–	O	x	M	O	O	O	x	O	O	O	CF	O
T	Martinez Mountain (USA)	4B	0.24	L	I	D	M	O	x	–	–	x	x	M	O	O	O	x	x	O	O	x	O
T	Blackhawk (USA)	2A	0.3	L	DR	K	M	–	O	–	–	x	x	M	O	O	O	x	O		O	x	O
TV	Aucanquilcha (USA)	4C	1(?)	T	U	Partially C	–	–	–	–	–	–	–	O	O	O	O	x	–	O	O	CF	O
TV	Chaos Jumbles (USA)	2B	0.026	I	U	K,D	M	–	x	–	–	O	O	M	O	O	O	x	x	O	O	x	O x
TV	Lastarria (Chile and Bolivia)	4D	0.091	± F	U	K	–	–	–	–	–	–	O	–	O	O	O	x	x	O	O	CA	O
TV	Mombacho (Nicaragua)	2C	1.2 (North); 1.88 (South)	L	U, DR	Uncof. at South, partly K at North	O	O	O	O	x	x	O	–	–	O	O	O	x	x	x	x	x
TV	Ollagüe (Chile and Bolivia)	4E	0.6 (?)	F	DR	Unconf.	O	O	O	O	–	x	–	O	O	O	x	O	x	x	O	CF	x
TV	Tetivicha (Bolivia)	5 A	–	F	I	K	–	–	O	–	–	–	O	–	O	–	O	O	–	O	O	x	x
TV	Llullaillaco (Chile and Argentina)	5B	1-2	F,T	U	K,2	–	O	O	–	–	–	–	O	O	O	O	O	x	O	O	CF	O
TV	Parinacota (Chile and Bolivia)	5C	6	I	PR	K,D	–	x	O	x	O	x	–	–	O	O	O	O	O	O	O	x	x
TV	Socompa (Chile and Argentina)	1	17	L,T	U at East, DR at West	D	O	O	O	O	x	x	x	O	O	O	O	x	O	O	O	CF	O
E	Olympus Mons (Mars)	5D	>500,000	L	U?	Unconf.?	–	–	–	–	–	–	–	–	–	O	O	x	–	O	O	CF	

Note: T—terrestrial; TV—terrestrial volcanic; E—extraterrestrial; L—lobate; F—fan shaped; T—tongue shaped; I—irregular; DR—distally raised; PR—proximally raised; U—uniform; Unconf.—Unconfined; K—confined; C—channelized; D—deflected; 2—divided; M—monolithologic; O—yes; x—not observed; dash (–)—data unavailable; CF—curved toward frontal regions; CA—curved toward amphitheater.

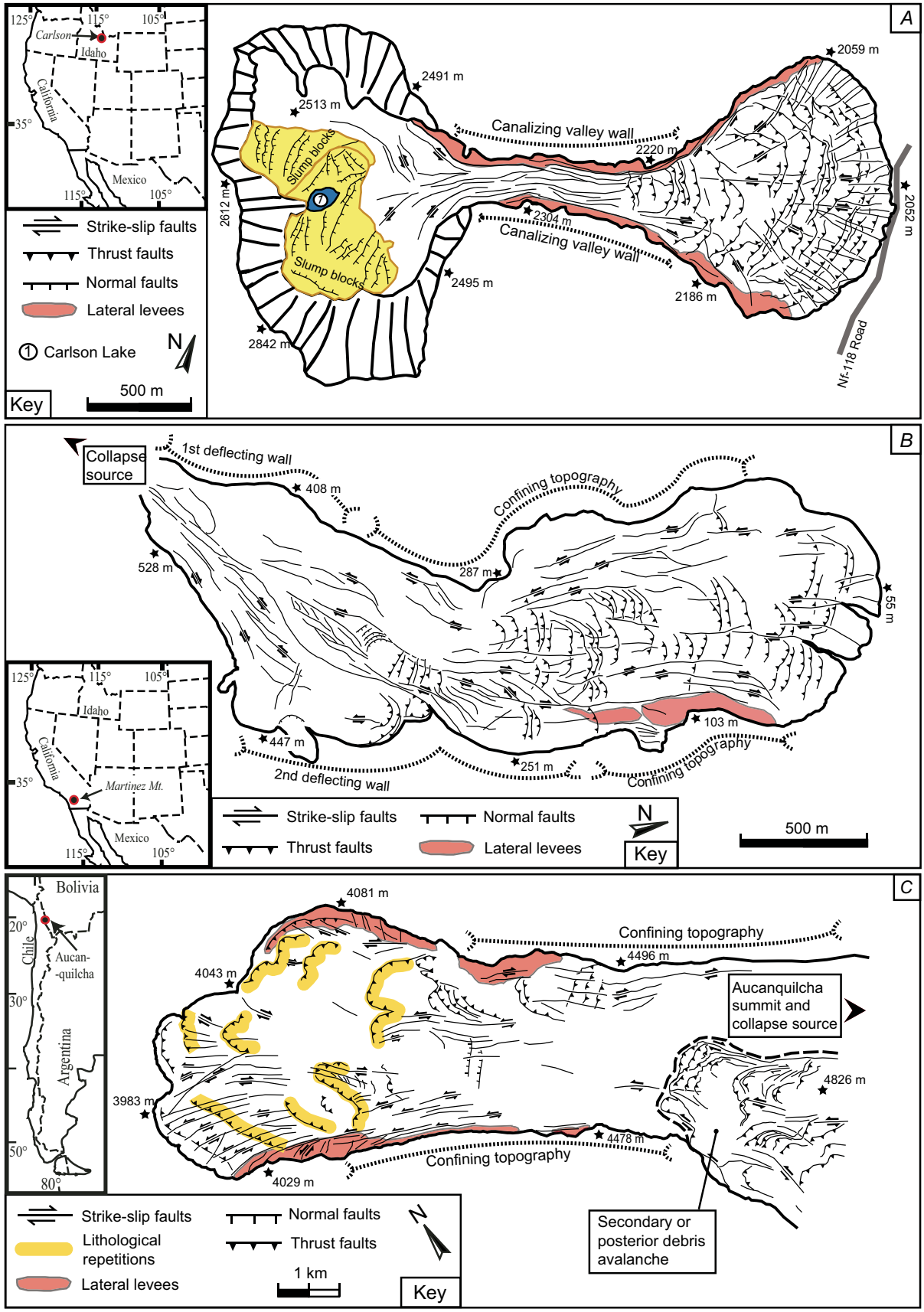

Figure 4 (*continued on next page*). **Structural maps. (A) Non-volcanic rockslide avalanche, Carlson (Idaho, USA). (B) Non-volcanic rockslide avalanche, Martinez Mountain (California, USA). (C) Volcanic rockslide avalanche, Aucanquilcha (Central Andes, Chile).**

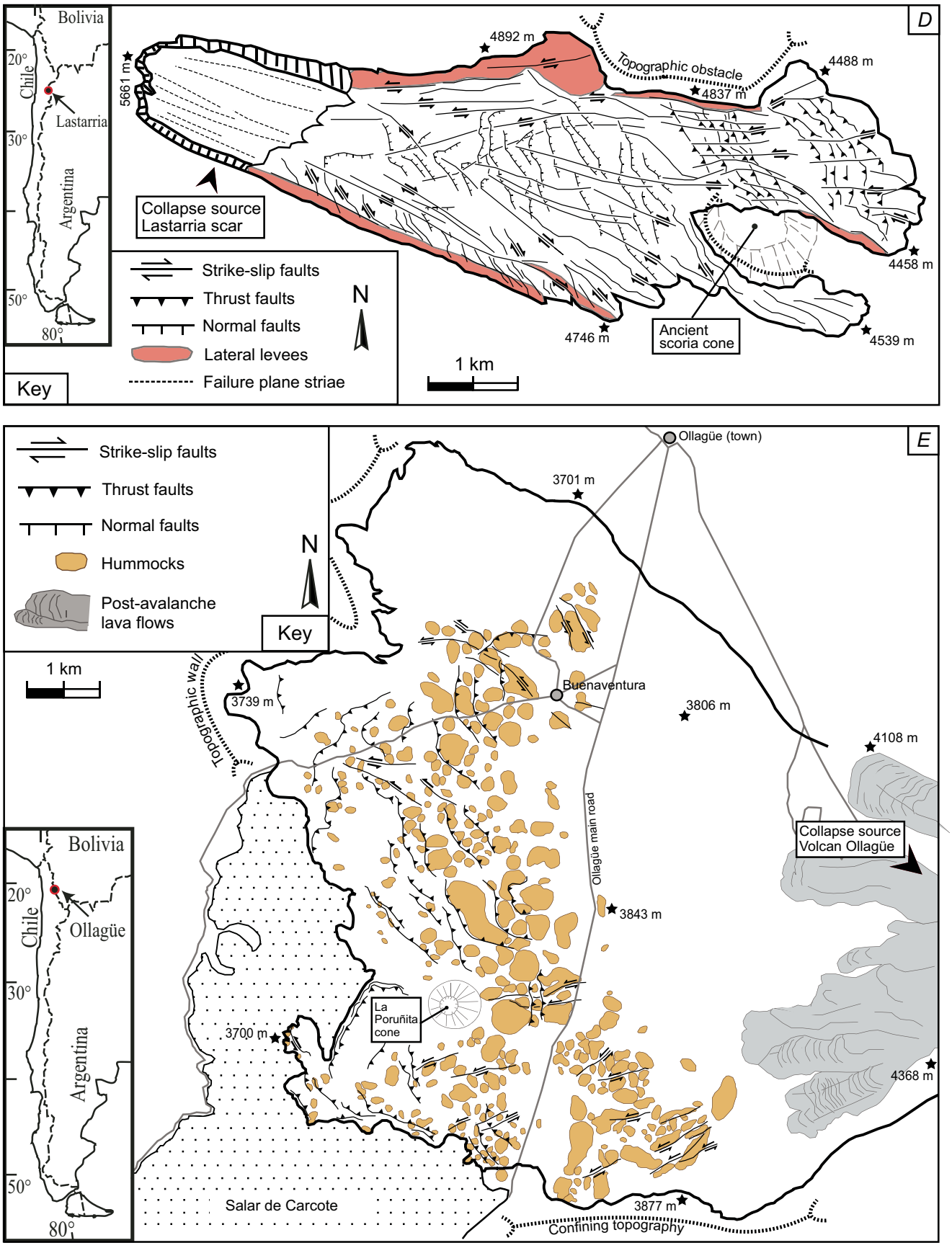

Figure 4 (*continued*). (D) Volcanic rockslide avalanche, Lastarria (Central Andes, Chile and Argentina). (E) Volcanic rockslide avalanche, Ollagüe (Central Andes, Bolivia and Chile).

are frequently unaffected by their emplacement (Shaller, 1991). Heim (1932) stated that this cohesive behavior arises from the presence of fine interstitial powders between larger particles in the mass.

Frequently, the deposits preserve original large-scale stratification. Heim (1932) was the first to make this observation at Elm, Switzerland. This represents strong evidence against intense large-scale mixing or turbulent transport. Many deposits also show a gross inverse grading that is explained either by stronger shearing and fragmentation occurring at the base, or clast segregation in a vibrating moving mass (Savage and Lun, 1988; Gray and Thornton, 2005; Shea et al., 2007). A certain fraction of substratum and/or bedrock can be torn, dragged, and incorporated by the mass during travel.

Structures

Faults are often seen at outcrop in rockslide avalanches, and may cut massive blocks, fractured blocks (block facies), and matrix breccias. Two examples from Socompa at outcrop are shown in Figures 1B and 1C. Many other examples have been given, including Glicken, (1998), Siebe et al. (1992), Clavero et al. (2002), Siebert et al. (2006), Shea et al. (2007), and Bernard et al. (2008). The faults record brittle deformation of incorporated parts of the intact edifice, as well as brittle deformation of the newly formed breccia. In nearly intact, resistant material, the faults can form discrete planes, with fault gauge and slickensides. In less resistant and brecciated material, they generally form broader shear zones (Figs. 1B, 1D). Such broader shear zones are common in unconsolidated and low resistance rocks, for example tephra, and are also formed in analogue models of volcano deformation using sand or other granular material (e.g., Merle and Borgia, 1996; Donnadieu and Merle, 1998; Merle et al., 2001).

On the surface of deposits, long ridges, escarpments, and troughs are the morphological expression of such faults (e.g., van Wyk de Vries et al., 2001). Normal faults are seen on the surface as sharp, generally straight escarpments, often with interior layers exposed, or exhumed, at the scarp base. Thrust faults form clear thrust anticlines, and are rounded, elongate ridges, often sinuous along strike. Strike-slip faults are lineations that have little topographic relief, but are often associated with pull-aparts, pop-ups, and splays. Normal and thrust faults

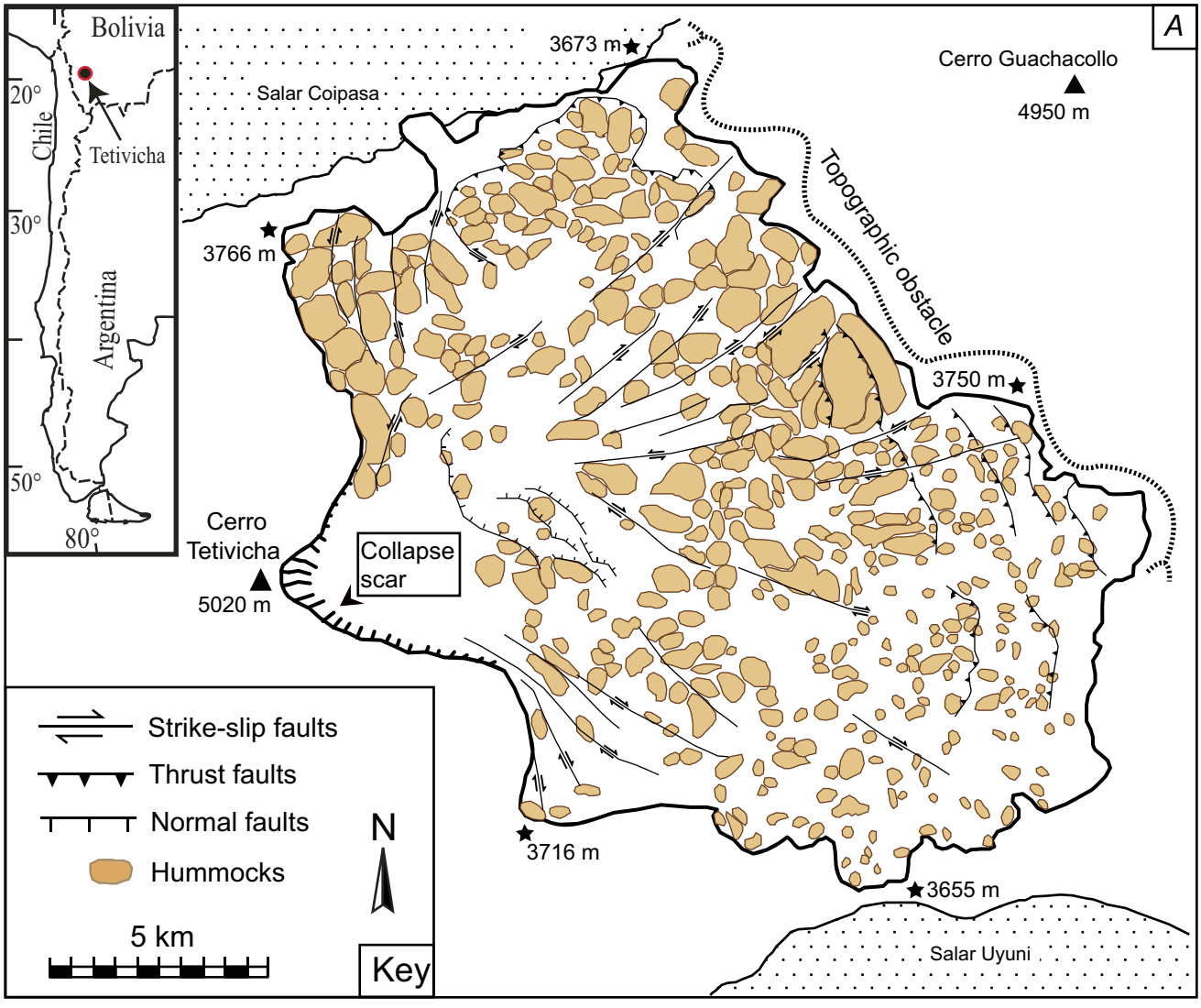

Figure 5 (*continued on next page*). Structural maps of volcanic rockslide avalanches. (A) Tetivicha (Central Andes, Bolivia).

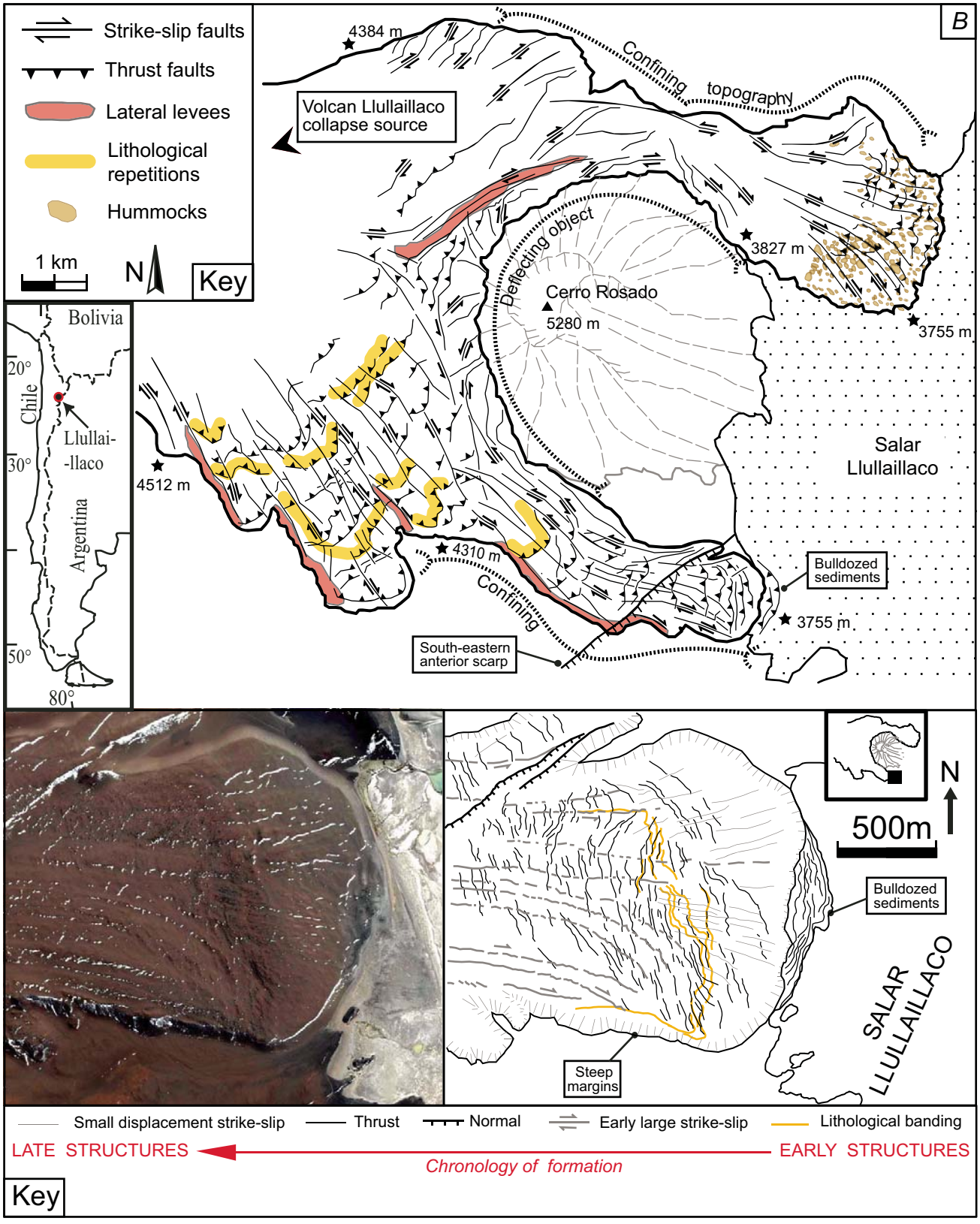

Figure 5 (*continued on next page*). **(B) Llullaillaco (Central Andes, Chile and Argentina).**

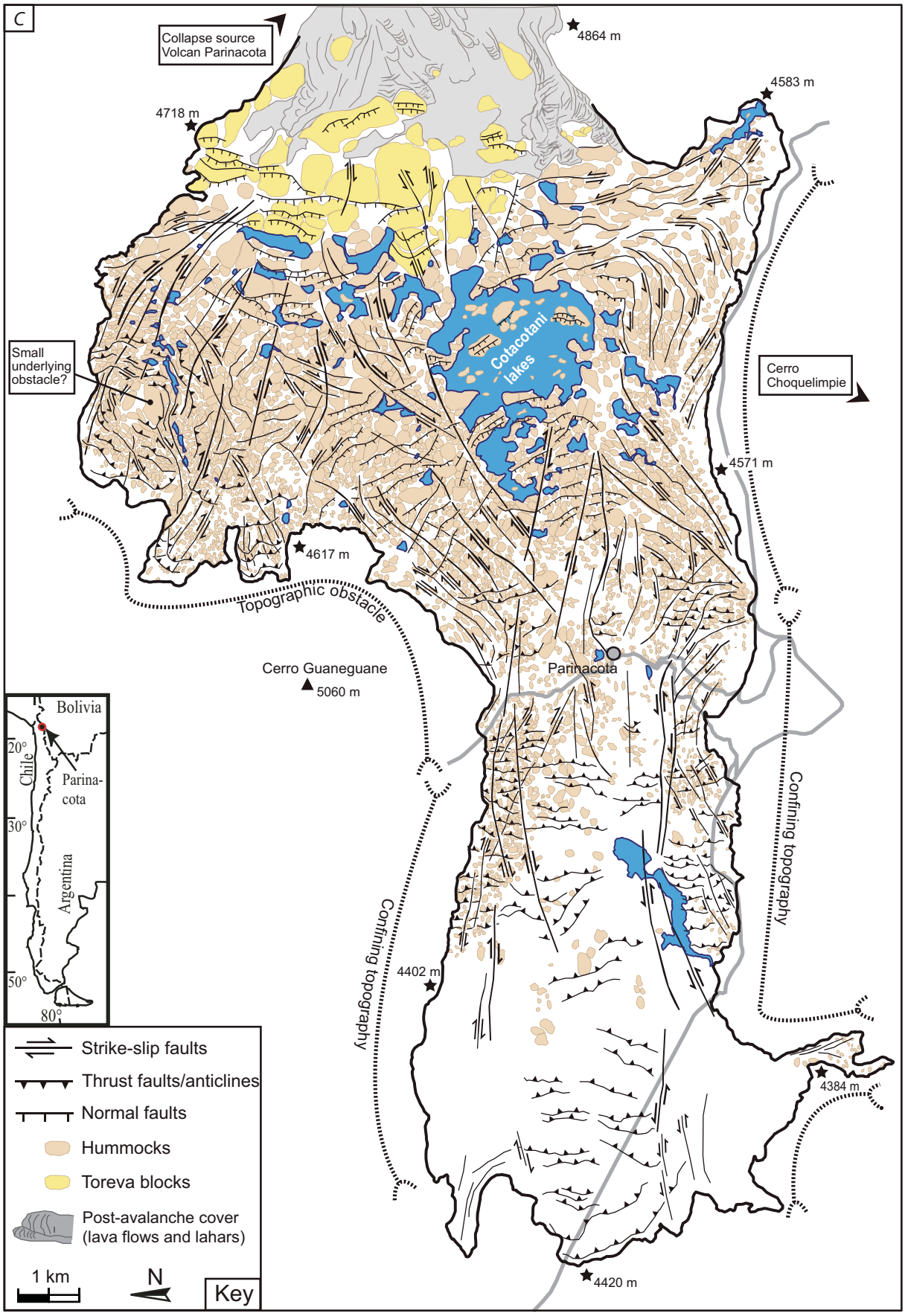

Figure 5 (*continued on next page*). **(C) Parinacota (Central Andes, Bolivia and Chile).**

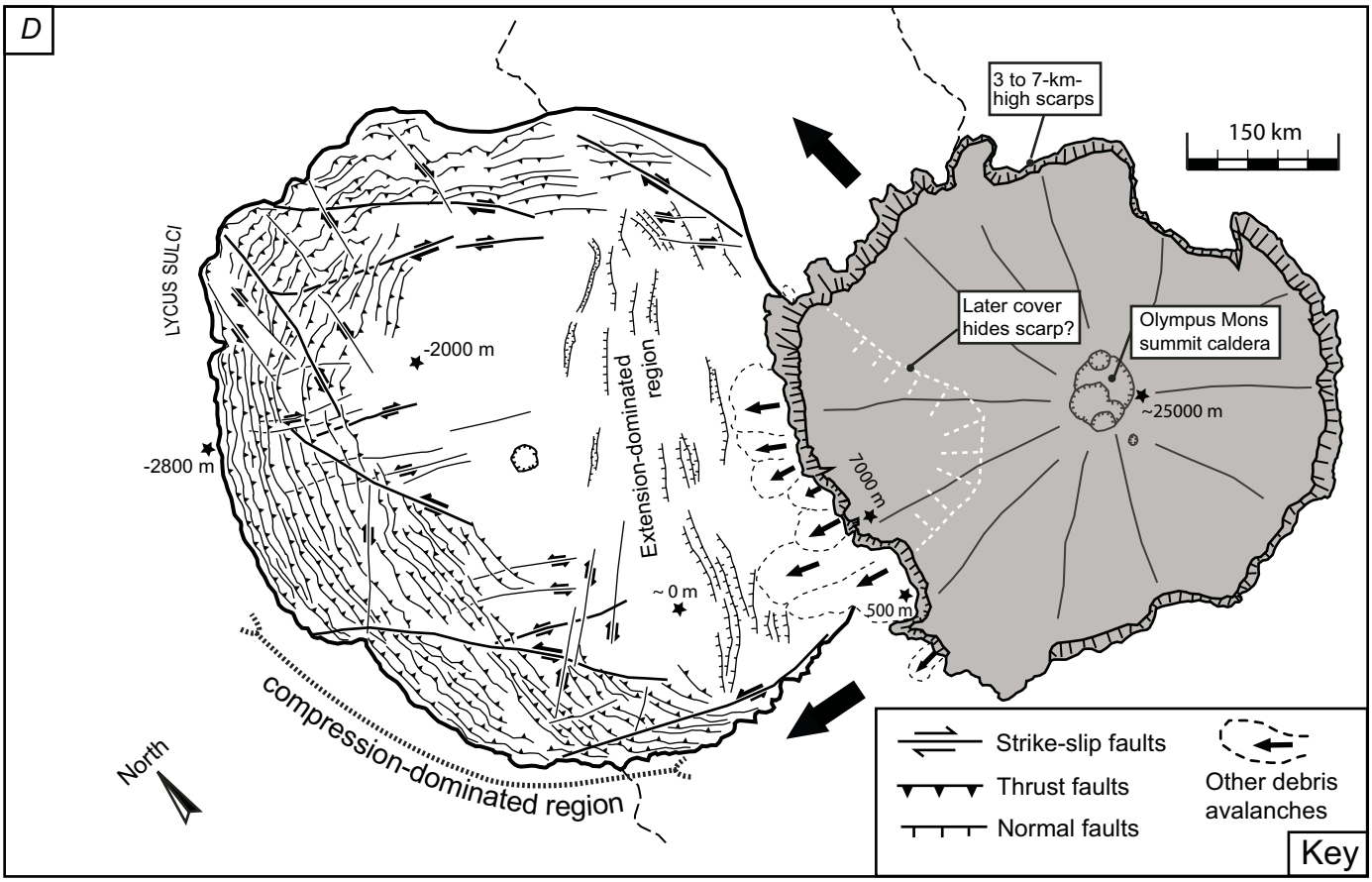

Figure 5 (*continued*). (D) Extraterrestrial Martian rockslide avalanche, Olympus Mons West (Mars).

often relay to strike-slip faults, showing coeval deformation. Good examples of strike-slip fault relays are seen on Socompa (Fig. 1) and some were analyzed in detail by Kelfoun et al. (2008). Probably the most spectacular example of faulting on a deposit surface is found at Socompa (Fig. 1), where the entire surface is cut by numerous generations of faults. These faults are seen in outcrop (Figs. 1B, 1C; van Wyk de Vries et al., 2001, 2002; Kelfoun and Druitt, 2005; Kelfoun et al., 2008), but are best mapped using aerial images and satellite photos due to the field observation scale. At Socompa, the upper part of the deposit shows normal, thrust, and strike-skip faults, while the lower part (which is infrequently exposed) shows horizontal banding, occasional diapirs, and fluid-like mixing textures compatible with a basal liquidized zone (van Wyk de Vries et al., 2001). Thus the surface behaved as a brittle crust (affected by faults) and the base as a liquefied and/or fluidized zone, along which the mass slid.

The faulting at Socompa shows distinct generations (Fig. 1), indicating that as the rockslide avalanche spread, fault sets were partly replaced by new surface structures. However, some large structural features, such as the Median Scarp (Fig. 1) and the major strike-slip faults remained active throughout the emplacement (van Wyk de Vries et al., 2002; Kelfoun et al., 2008). Normal faults are generally located toward the central or proximal regions of the deposits, while thrust faults mostly appear in distal regions (this is true for all our observed rockslide-avalanche deposits, except Mombacho North and South, which do not display thrust faults). Thrusts may generate vertical recurrence of the stratigraphic succession (Fig. 1C; Socompa, Aucanquilcha, Llullaillaco, and Ollagüe).

Hummocks are also an expression of strong stretching around blocks by faults (Glicken, 1998; Glicken et al., 1981; Voight et al., 1981; Shea et al., 2007). Numerous rockslide-avalanche surfaces exhibit rounded or conical hummocks with circular and/or elliptic bases (e.g., Mombacho, Llullaillaco Northern subunit, Parinacota, Ollagüe, and Tetivicha) and sizes frequently reaching one hundred meters. According to Voight et al. (1981) and Glicken et al. (1981), hummocks result from the creation of horsts and grabens during transport and spreading. Slump blocks or Toreva blocks (e.g., Carlson, Blackhawk, Parinacota, Socompa) are massive portions of intact material, which slid and underwent slight backward rotational movements without being significantly brecciated (Reiche, 1937; Wadge et al., 1995; van Wyk de Vries et al., 2001; Clavero et al., 2002). Longitudinal or oblique ridges may be observed oriented parallel or oblique to transport, respectively, while transversal ridges show perpendicular directions. Arched ridges are curved concavely or convexly transversal to slope direction, while marginal accumulation ridges (or "bulldozer facies"; Belousov et al., 1999) form when dragged material piles up at the borders of the rockslide avalanche during travel. The rockslide avalanche's underlying substratum is often folded, eroded, or faulted by the moving rock mass. Similar to the rockslide avalanche, the substratum may be affected by slip surfaces or imbricate ridges (Belousov et al., 1999; Clavero et al., 2005).

ANALOGUE MODELING OF ROCKSLIDE AVALANCHES

Most models have focused on the transport physics and emplacement dynamics of rockslide

avalanches, and some have tried to model them numerically directly (e.g., Kelfoun and Druitt, 2005) or indirectly (e.g., Campbell, 1989, 1995; Pouliquen and Renaut, 1996; Staron et al., 2001). While analogue modeling is used extensively in numerous domains of geology to study structures, it has not been applied in this way to rockslide avalanches. The current literature on analogue models of rockslide avalanches was comprehensively summarized by Pudasaini and Hutter (2007). Ramps of differing shape and dimension have been used with various granular materials. However, no model has yet been designed to reproduce the surface morphology and structure or explore the internal distribution of stratified material. In none of the described models are faults seen, and many of them have deposit thickness distributions very different from natural examples. For example, the experimental deposits in Denlinger and Iverson (2001) and Iverson and Denlinger (2001) are piled up in a mound at the base of the slide slope, a distribution found in small rockslides but not in larger events like those studied here. While such models can be useful for verifying physical models of granular flow, they are not so valuable for exploring the kinematics of rockslide analogues. In particular, they do not reproduce the observed structural morphology of the surface of natural events.

Modeling large-scale landslides poses numerous scaling problems: scale reduction inevitably creates the loss of a fundamental property: the volume. Consequently, the only ways to obtain equivalent runout at smaller scales is to inject a certain additional quantity of energy to the system or to lubricate the basal sliding plane. Therefore, laboratory experiments without this external energy contribution or basal friction reduction will not be realistic in modeling high horizontal travel for a given fall height. Even so, with a reduced basal friction, low runout experiments can be used to approach the problem by focusing on deposit structure formation and deposit morphology, and so to investigate the transport type and deformation chronology (kinematics) from slide initiation to material runout. This is our approach here. We stress that the models developed here do not attempt to explore the physical processes of the low-friction basal décollement: this is simply reproduced as a smooth sliding plane. Thus, the study concentrates on the kinematics and structural development of the upper brittle layer. As the physics of the low-friction basal layer are still unknown, but the mechanisms of fault formation are better constrained, we believe this is a suitable approach. In addition, the surfaces of rockslide avalanches provide abundant structural data that can be compared with the models, while basal layers are harder to study.

This type of "structural to dynamics" approach has been used in tectonic and volcano-tectonic analogue models for a long time (e.g., Merle and Borgia, 1996, and references therein) and it can provide the necessary kinematic and structural information to investigate motion. Once such kinematic information is established, a second and future step would be to investigate the dynamics of the basal layer. Here the basal layer is simulated by a low-friction surface, which provides an analogue for the natural slide layer. Because the exact process or combination of processes that cause low friction in a sliding mass are still not completely understood, this approach provides a simple analogue to whatever low-friction conditions actually exist. The approach is similar to the numerical simulations of Kelfoun and Druitt (2005) that vary the coefficient of friction in and at the base of their simulated rockslide avalanche.

A rockslide avalanche involves a gravity-driven downward slide of rocky fragments that spreads until the initial kinetic energy acquired from the fall is entirely dissipated by intergranular interactions and basal friction. As fault structures may only appear in the frictional granular regime, the modeling of rockslide avalanches requires a system that can realistically reproduce analogues to such a state. In this study, we assume a plug-flow type of configuration, where the main body suffers a different deformational regime than the base (e.g., Kelfoun and Druitt, 2005). It is therefore crucial to stress that our intention is to model a granular slide (dominantly frictional regime), in which brittle-type structures can form, rather than a granular flow (dominantly collisional regime).

Sand has been often used in analogue modeling of volcano-tectonic phenomena (Merle and Borgia, 1996; van Wyk de Vries and Borgia, 1996; van Wyk de Vries and Merle, 1996; van Wyk de Vries and Francis, 1997; Donnadieu and Merle, 1998; Davies et al., 1999; Merle and Donnadieu, 2000; Donnadieu, 2000; Lagmay et al., 2000; Merle et al., 2001; Cecchi et al., 2004; Oehler et al., 2005; see also Pudasaini and Hutter, 2007, and references therein). Sand has an internal friction angle similar to most natural rocky materials and a low dry-state cohesion that make it an appropriate tool for laboratory-scale reduction. However, most deposits enclose rock fractions varying from the micron to the multimeter scale, and by definition, granular media must have diameters >~80–100 μm (Duran, 1997). Because the sand used for laboratory experiments ranges from 60 to 600 μm, scale reduction inevitably entails a sacrifice of end-member fractions that are present in nature.

Any particle with a diameter <100 μm is classified as powder, the behavior of which differs significantly from dry granular materials. Several characteristics modify their properties, such as electrostatic interactions and the strong effect of humidity. The chosen analogue material must therefore be mostly composed of particles >100 μm. Our sand is 99.7% silica, with 99.3% above 100 μm, its elasticity is equivalent to most silicate materials, its internal friction angle is 33°, and its density is ~1500 kg m^{-3}. Numerical and/or analogue experiments frequently choose to use spherical beads in their initial conditions. This is, however, not the case in natural deposits, where fragments are more angular than rounded; hence our choice of nonspherical sand particles rather than glass beads. Sand layers are dyed with paints of different colors and can be used accordingly as markers without modifying the granular medium properties (Donnadieu, 2000). The cohesion can be increased by adding an interstitial fluid, such as water (capillary cohesion; Hornbaker et al., 1997), or by adding cohesive powder materials, such as plaster. Note that the addition of very small amounts of water does not simulate saturation and processes such as lahar generation.

Choice of Model

We chose a geometrically simple model representing the failure, transport, and emplacement plane. The common characteristic in every sliding surface is slope variation. Failure usually occurs on a surface slope that is above or equal to the internal friction angle of the collapsing materials. These materials accelerate until they reach a gently sloped depositional surface. Following these simple observations, our laboratory model is a curved ramp built with a flexible aluminum sheet (4 mm thick, 150 cm wide, and ~300 cm long), in which the initiation and deposition slopes could be modified (Fig. 6A). Other materials previously tested (e.g., varnished wood, Plexiglas, or PVC) are less convenient because they induce undesired electrostatic interactions with the sliding material. The basal friction angle of the aluminum sheet is relatively low, 24°, measured by progressively tilting the surface with a pile of grains of known thickness on it. Note that in choosing a low-friction surface we are replicating the equivalent of a highly deformed simple shear basal layer in a plug-flow–type configuration. Three different ramps (later referred to as models 1, 2, and 3) were tested using initiation slopes between 45° and 30° and deposition slopes varying between 0° and 18° (Fig. 6B). Three source boxes of different volumes are used (1250 cm^3, 2600 cm^3, and 5250 cm^3) preserving a constant thickness

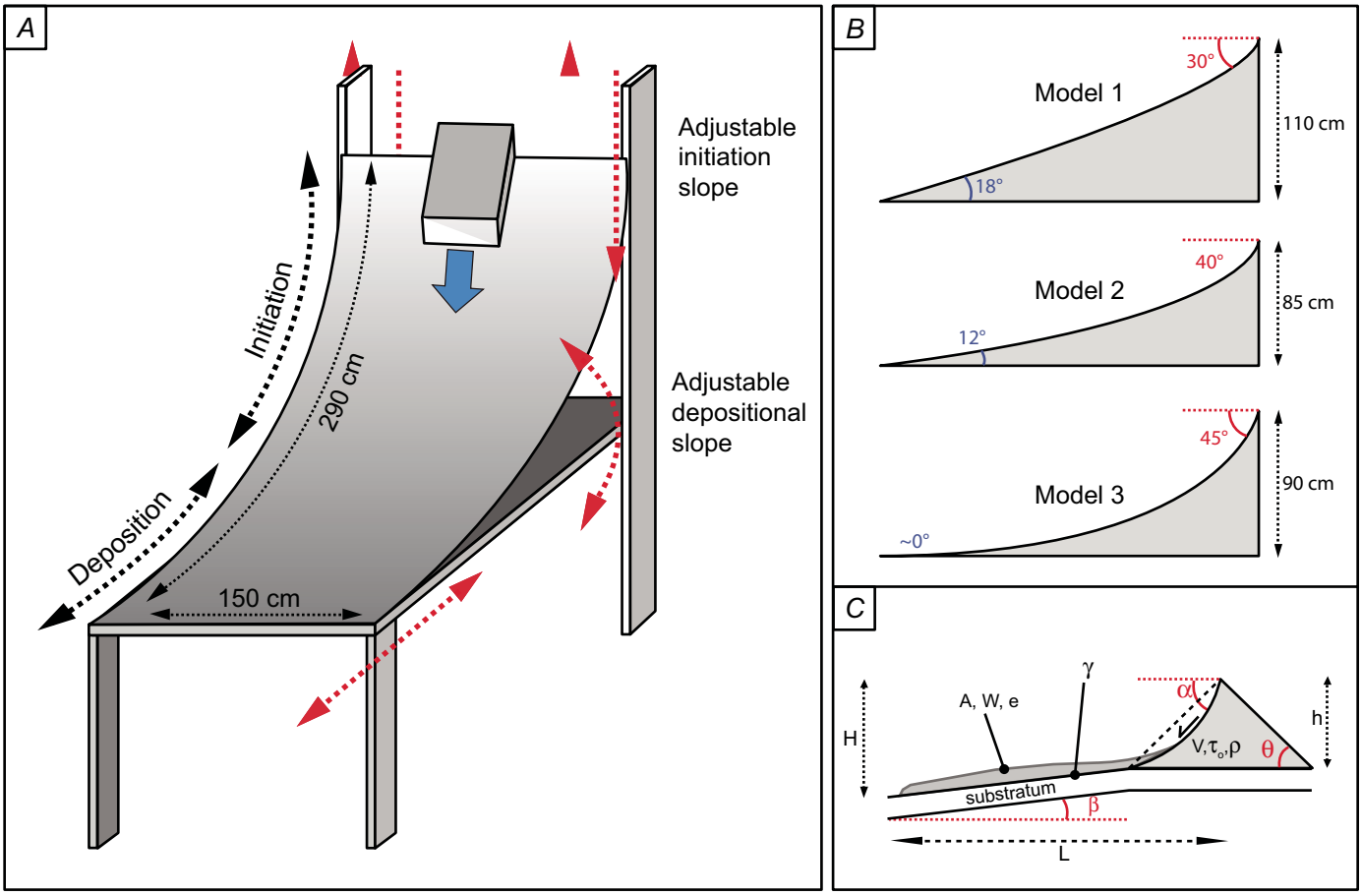

Figure 6. (A) Illustration of the ramp used for running scaled laboratory experiments. (B) Different ramp configurations, models 1, 2, and 3. (C) Main variables used in dimensioning our analogue model; see Table 2 for terms and values.

of 5 cm. A box-type geometry was preferred over a wedge or a bowl-shaped initial collapse structure, because its simple symmetry allows better tracking of deformation and changes in shape geometry. The boxes can be closed from above and possess a frontal trapdoor. The restriction of particle motion when manipulating the boxes is crucial; when the latter are tilted following the initiation plane, the sand must not move until the frontal trap is opened. This is ensured by a compressive lid tightly closed and tied to the lower part of the source boxes. The main advantage of the system is that it allows the emplacement of slope-parallel material strata that stay in place when tilting the boxes. This setting gives the possibility to follow the deformation that affects different layers, and characterize the structures formed (e.g., thrust, normal, or strike-slip faults).

Scaling

In order to guarantee maximum similarity between reality and laboratory analogue models, certain geometric and dynamic parameters must be scaled. This fundamental step allows determining of the conditions necessary to ensure proportional correspondence between forces acting in nature and those acting in a laboratory environment (Ramberg, 1981). Accordingly, we define eight dimensionless numbers that serve to compare dynamic and geometric features in both nature and the laboratory.

Nearly all physical quantities can be expressed with the primary dimensions of length [*L*], mass [*M*], and time [*T*], except for those that are said dimensionless and do not require unit specifications. The following three groups of variables affect the system (Fig. 6C; Table 2).

1. Variables related to the deposit geometry and the sliding environment (source and depositional surface): horizontal runout *L*, deposit thickness *e*, area *A*, width *W*, total fall height *H*, fall height from source to beginning of depositional surface *h*, the failure surface average slope α, the depositional surface average slope β, and the initial volume *V*.
2. Variables associated with intrinsic material properties: density ρ, cohesion τ_o, the internal friction angle θ.
3. Dynamic variables: the basal friction angle γ, flow velocity *u*, and gravity g.

The variables in 2 and 3 are very poorly understood, or even unknown in natural rock-slide avalanches, which limits the scaling possible for dynamic comparisons. However, general statements can be made with caution about the response of the models to changing parameters that may be applicable to natural cases. The geometrical and structural parameters can be handled with the most confidence, as these are best known in natural examples, and best constrained in the models. Both model and natural prototypes deform in the frictional regime, which is strain rate insensitive. Thus, as long as the models remain in this regime, velocity and strain rate scale differences will not be significant (see discussion in Middleton and Wilcock, 1994). These parameters are discussed in the section on deformation and velocity evolution.

TABLE 2. LIST OF SCALING VARIABLES INVOLVED IN ROCKSLIDE AVALANCHE MOTION, EMPLACEMENT, THEIR DIMENSIONS AND THEIR VARIATION RANGE BOTH IN NATURE AND IN THE ANALOGUE EXPERIMENTS

Variables	Dimensions	Nature	Model	Scaling intervals
L—avalanche runout	[L]	0,1–100 km	0,001-0,003 km	L*=Ω*.T*=1/300-1/15000
H—total fall height	[L]	500–5000m	~1m	1/100-1/4000
h—fall height before arrival on depositional slope	[L]	500–3000m	0,5–0,9m	1/500–1/6000
W—deposit width	[L]	1–20000m	0,3–0,7m	1/3–1/30000
A—covered area	[L^2]	0,1–700 km^2	~1m^2	1/10^6–1/10^8
V—volume	[L^3]	0,001–100 km^3	1,2.10^{-12}–5,25.10^{-12} km^3	~1/10^{12}
e—deposit thickness	[L]	5m–300m	0,005–0,03 m	1/5000–1/10000
u—avalanche velocity	[LT^{-1}]	20–100m.s^{-1}	1 m.s^{-1}	Ω*=1/20–1/100
Ø— clast diameters	[L]	60µm–50m	60–600µm	1/1–1/70000
ρ—material density	[M L^{-3}]	1300–2600 kg.m^{-3}	1300–1600 kg/m^{-3}	1/2–1/1
g—gravity	[L T^{-2}]	9,81 m.s^{-2} on earth	9,81 m.s^{-2}	1/1
θ—internal friction angle	–	30°	33°	1/1
t—emplacement time	[T]	30–500 sec	2–3 sec	T*=1/15–1/150
γ—basal friction angle	–	0–30°	24°	~1/1
α—failure plane average slope	–	20–50°	30–45°	~1/1
β—depositional surface average slope	–	0–20°	0–18°	~1/1
τ_o—cohesion	[M $L^{-1}T^{-2}$]	2000–100000 Pa	0–250 Pa	1/400–1/2000

The number of variables acting on such a complex phenomenon is large; hence to allow a simple and well-defined model, certain important variables must be selected. For our experiments we consider that essential variables are tan(α), tan(β), tan(θ), *L*, *H*, *A*, *V*, τ_o, ρ, and g. Other variables do not change as significantly in experiments and thus are taken as constants. This gives ten important variables, three of which are selected as repetitive variables, each showing independent dimensions (i.e., no variable can be expressed by the product of the two others) and whose behavior is less interesting for the study than the others (Middleton and Wilcock, 1994). The three repetitive variables are *V*, ρ, and g. Combining *L*, *H*, *A*, *V*, τ_o, tan(α), tan(β), tan(θ) with them produces our dimensionless pi (Π) numbers. Tan(α), tan(β), tan(θ) are expressed as $[L]\cdot[L^{-1}]$ and are dimensionless. Thus the three first pi numbers are: $\prod_1$ = tan(α), or dimensionless acceleration; $\prod_2$ = tan(β), or dimensionless deceleration; and $\prod_3$ = tan(θ), which stays constant and will be ignored.

For the length scaling, we start with the function: *f(L)* = *L*,*V*, ρ, g. *L* is given an exponent of 1, the dimensions are:$[L]^1$ $[L^3]^a[ML^{-3}]^b[LT^{-2}]^c$. For the products to be dimensionless, the sum of the exponents from [*L*], [*M*], [*T*] must be 0:

$1 + 3a - 3b + c = 0$ for *L*

$b = 0$ for *M*

$-2c = 0$ for *T*, $c = 0$

hence $a = -\frac{1}{3}$.

In this way we define:

$$\Pi_4 = \frac{L}{V^{\frac{1}{3}}}, \quad (1)$$

or dimensionless runout. Scaling of τ_o is as follows:

$$f(\tau_o) = \tau_o, V, \rho, g;$$

we choose to give τ_o the exponent 1. The dimensions are:

$$[ML^{-1}T^{-2}]^1[L^3]^a[ML^{-3}]^b[LT^{-2}]^c$$

$-1 + 3a + 3b + c = 0$ for *L*

$1 + b = 0$ for M, so $b = -1$

$-2 - 2c = 0$ for *T*, so $c = -1$

hence $a = -\frac{1}{3}$.

Thus:

$$\Pi_5 = \frac{\tau_0}{\rho g V^{\frac{1}{3}}}. \quad (2)$$

can be considered the dimensionless resistance. To those five pi numbers we can add:

$$\Pi_6 = \frac{H}{V^{\frac{1}{3}}}, \quad (3)$$

equivalent to dimensionless initial energy; and

$$\Pi_7 = \frac{A}{H^2}, \quad (4)$$

equivalent to dimensionless area. The inverse of Π_6 could be considered as a factor of dimensionless volume:

$$\Pi_6' = \Pi_6^{-1}. \quad (5)$$

Calculating variation intervals for these values in the model and in nature (Table 2) allows testing for similarity. Figure 7 shows that our model Π numbers overlap with those from natural deposits, with a slight overestimation of dimensionless resistance Π_5 in the models. This is expected, as our basal friction is not significantly lower than in nature, while the driving force is greatly reduced.

In the models the quantified elements are the geometric parameters length, width, thickness, as well as structure orientation and structure dip. Other morphological parameters are described qualitatively, such as deposit geometry and the presence of structural features like hummocks or lateral levees. We tested the influence of initiation and deposition slopes, material cohesion, volume, confinement, the presence of an unconsolidated substratum, and particle size. Filmed experiments serve to analyze the evolution of deformation (kinematics) and flow velocity. The objective of our model is not to reproduce the extreme runout of natural events, but the formation and evolution of structures, in order to gain insights into their kinematics. Even so, the ramp used has sufficiently low basal friction to permit *H*/*L* values as low as 0.33.

Model Reproducibility

Before results can be interpreted, experiments must have an acceptable reproducibility and show the same geometric, morphologic,

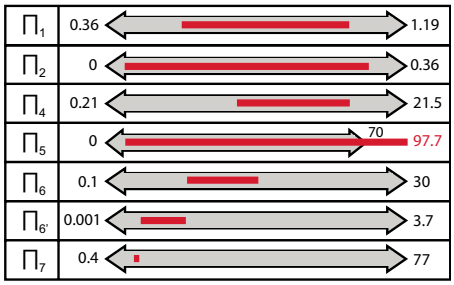

Figure 7. Compared Π number variation ranges between the model and nature. The lower values for each environment are always on the left and upper values are on the right side. Note that the Π number value intervals from the model are generally well included into the Π number value intervals from nature, except for Π_5, which reaches higher values in the model than in nature.

and dynamic characteristics for identical starting parameters. Thus standard experiments were conducted before each set of runs to ensure good reproducibility. In addition, for each experiment two or three reiterations were made to average measurements. To avoid cohesion changes due to variations in ambient humidity, each group of parameters was tested on the same day. After each experiment, the sliding surfaces were cleaned with an antistatic product to ensure constant basal friction and avoid parasitic superficial electrostatic charges. Each time the boxes were filled, careful manual shaking guaranteed the most compact particle arrangement. This minimized intergranular spaces and ensured minimum grain remobilization during tilting. A total of 50 experiments were characterized in detail while others served as standards.

RESULTS

Experimental results (geometric measurements, structural characteristics, comments) are reported in Supplemental Table 1[2].

Standard Experiment

The no. 1 ramp had an initiation slope α = 45°, a horizontal emplacement slope β = 0° and a material volume of 2600 cm^3. The obtained deposit (Fig. 8A) had an oval lobate shape, with lateral levees, a maximum length of 241.5 cm, a maximum width of 52.5 cm, and a thickness of 1.85 cm. The profile was distally raised, the *H*/*L* ratio was 0.37, and the mass covered an area of ~4500 cm^2. Analysis of the deposits shows that numerous ridges appeared on the surface; some were parallel to oblique to transport direction, depending on their location along the central axis or near the lateral levees, respectively; others were transverse and slightly convex toward the deposit toe.

Characterization of Recurrent Structures

Initial material stratification allowed distinction of structures. After transport and emplacement, the sand mass preserved general stratigraphic order, but recorded significant deformation. Transverse and longitudinal cross sections (Figs. 9 and 10) show that thrust faults (or folds) mostly affect distal zones of the deposit; their dips vary between 15° and 60° and decrease toward the front (cross-sections, Figs. 10A, 10B and 11A). On the deposit surface, these were expressed as closely packed low-amplitude ridges. Lithological repetitions also appeared as alternating colored stripes at the surface with orientations parallel to thrust structures. Close to the lateral borders, structures had a strike-slip component. On a slide-surface parallel cut (Fig. 9A), the lateral strike-slip zones were easily distinguished. They showed subvertical to 45° dips toward the center of the deposit, and their orientations varied from parallel to oblique (±35°) to transport direction. Slight frontal digitations (Figs. 8A, 8B, 8H, 8J) corresponded to zones displaced by strike-slip structures. Similar to the standard experiment, the profile was distally raised. Proximal zones were affected by normal faults (Figs. 9C, and 10C, 10D) that were usually more difficult to distinguish than thrust faults because the deposit was much thinner. At the back of certain deposits, small isolated transport-parallel ridges (or striae) could be observed (Figs. 8D, 8F, 8G).

Effect of Volume

Figure 11B plots deposit length *L* as a function of initial volume (1250, 2600, or 5250 cm^3). This relation demonstrates that an increase in initial volume also increased *L* for a constant *H*, thus slightly decreasing the *H*/*L* ratio. This effect was more pronounced from 1250 cm^3 to 2600 cm^3 than from 2600 cm^3 to 5250 cm^3. Also, volume increase amplified structure density and visibility (Fig. 8J): while sporadic and indistinct at 1250 cm^3, structures were frequent and well marked at 5250 cm^3. The surface ridge wavelength was nevertheless similar, unaffected by volume changes.

Effect of Cohesion

Cohesion can be increased in the initial material in two ways, resulting in both cases in a lobate deposit with shorter lateral levees than when using normal sand. Increases in cohesion were achieved by adding a certain proportion of plaster to the sand mixture. The effect of plaster content on *L*, and therefore *H*/*L*, is reported in Figure 11C. Plaster varied between 1% and 0% in our experiments, corresponding to cohesions of ~2–10 Pa (Donnadieu, 2000). The effect of adding plaster was apparent from the smallest amount: it decreased *L*, therefore increasing considerably *H*/*L*. Adding more plaster, however, did not significantly modify the rockslide-avalanche behavior. A rheological threshold was thus reached. Moreover, if pure plaster is sandwiched between cohesionless layers, the deposit shows geometrical characteristics (e.g., *A*, *L*, *H*/*L*, *e*, *W*) similar to the standard experiment. On the deposit surface, however, lumps comparable to hummocky topography emerge (Fig. 8C), large in central zones and smaller toward lateral edges.

Alternatively, cohesion may be increased by introducing very small quantities of water into the initial material (capillary cohesion); this results in even stronger bonds between grains than previously (cohesion >200 Pa). The humid layer also produced hummocky topography on the deposit surface (Fig. 8D). This time, however, hummock size remained almost constant throughout the deposit. In cross section (Fig. 10C), the brittle humid layers showed boudinage structures between normal sandy layers and had migrated upward. Whether humid sand or plaster was used, each hummock was structurally isolated from the others and formed its own topographic domain. In both cases the cohesive layer can be placed on top or between noncohesive layers, but never at the base, or else the mass is prematurely stopped.

Effect of Confinement

A rockslide avalanche can be confined and/or channelized in two ways: during its downward movement along the failure surface by its own amphitheater edges, or subsequently by

[2]If you are viewing the PDF of this paper or reading it offline, please visit http://dx.doi.org/10.1130/GES00131.S1 (Table S1) or the full-text article on www.gsajournals.org to view Supplemental Table S1.

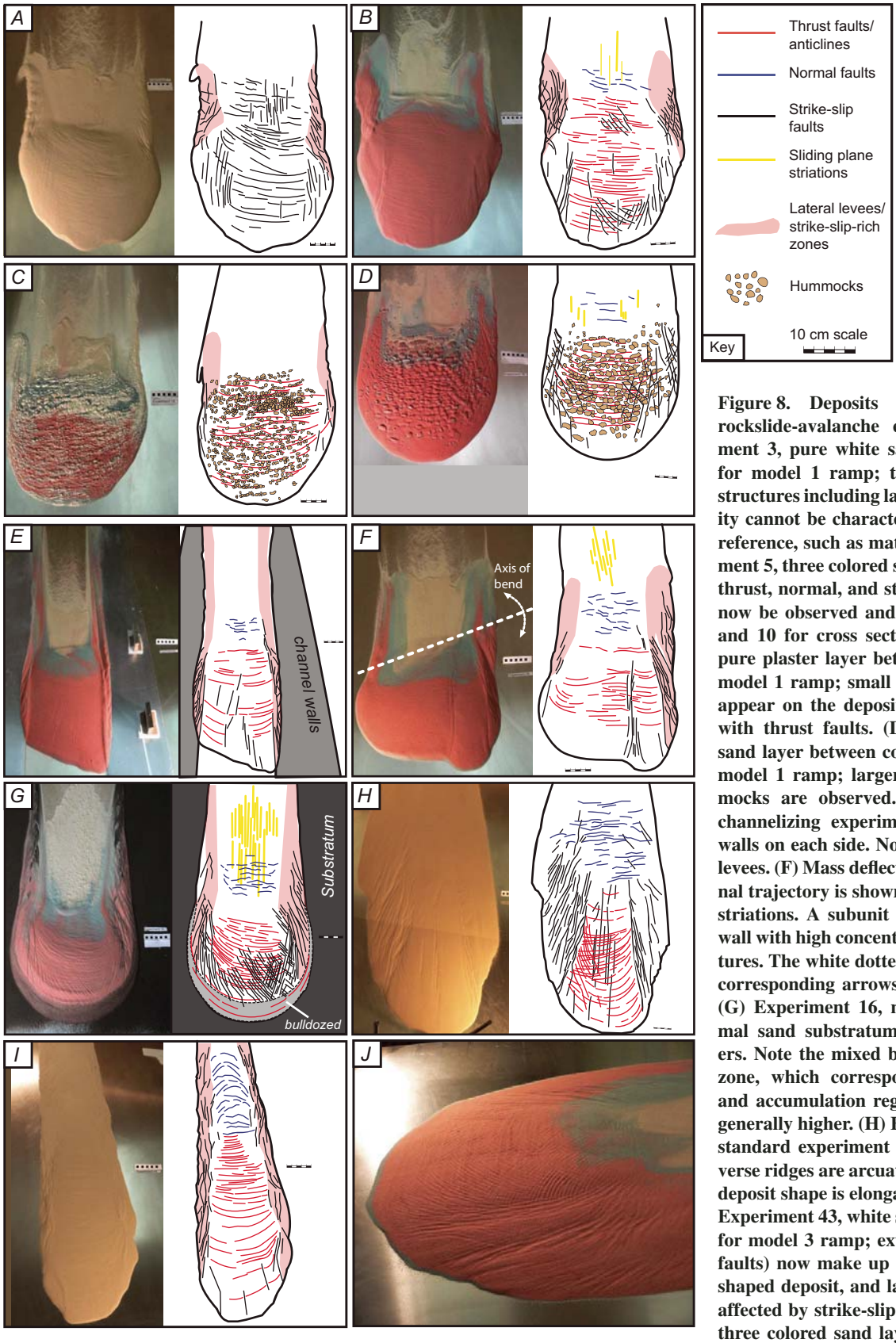

Figure 8. Deposits from laboratory scaled rockslide-avalanche experiments. (A) Experiment 3, pure white sand, standard experiment for model 1 ramp; the surface shows various structures including lateral levees, but the majority cannot be characterized due to the lack of a reference, such as material layering. (B) Experiment 5, three colored sand layers, model 1 ramp; thrust, normal, and strike-slip fault systems can now be observed and characterized (see Figs. 9 and 10 for cross sections). (C) Experiment 14, pure plaster layer between colored sand layers, model 1 ramp; small and numerous hummocks appear on the deposit surface, roughly aligned with thrust faults. (D) Experiment 15, humid sand layer between colored normal sand layers, model 1 ramp; larger and better-defined hummocks are observed. (E) Rockslide-avalanche channelizing experiment with valley-like sidewalls on each side. Note the well-marked lateral levees. (F) Mass deflecting experiment. The original trajectory is shown by the acceleration plane striations. A subunit forms near the deflecting wall with high concentrations of strike-slip structures. The white dotted line shows the bend, and corresponding arrows show the bend direction. (G) Experiment 16, model ramp 1, black normal sand substratum under colored sand layers. Note the mixed black and red sand frontal zone, which corresponds to important thrust and accumulation regions. Fault density is also generally higher. (H) Experiment 25, white sand, standard experiment for model 2 ramp. Transverse ridges are arcuate toward the front and the deposit shape is elongated with a lobate front. (I) Experiment 43, white sand, standard experiment for model 3 ramp; extensive structures (normal faults) now make up almost half of the tongue-shaped deposit, and lateral levees are extremely affected by strike-slip faults. (J) Experiment 31, three colored sand layers, model 1 ramp, highest initial volume; the density and/or concentration of structures increases with volume. For all experiments, 10 cm scale is on right.

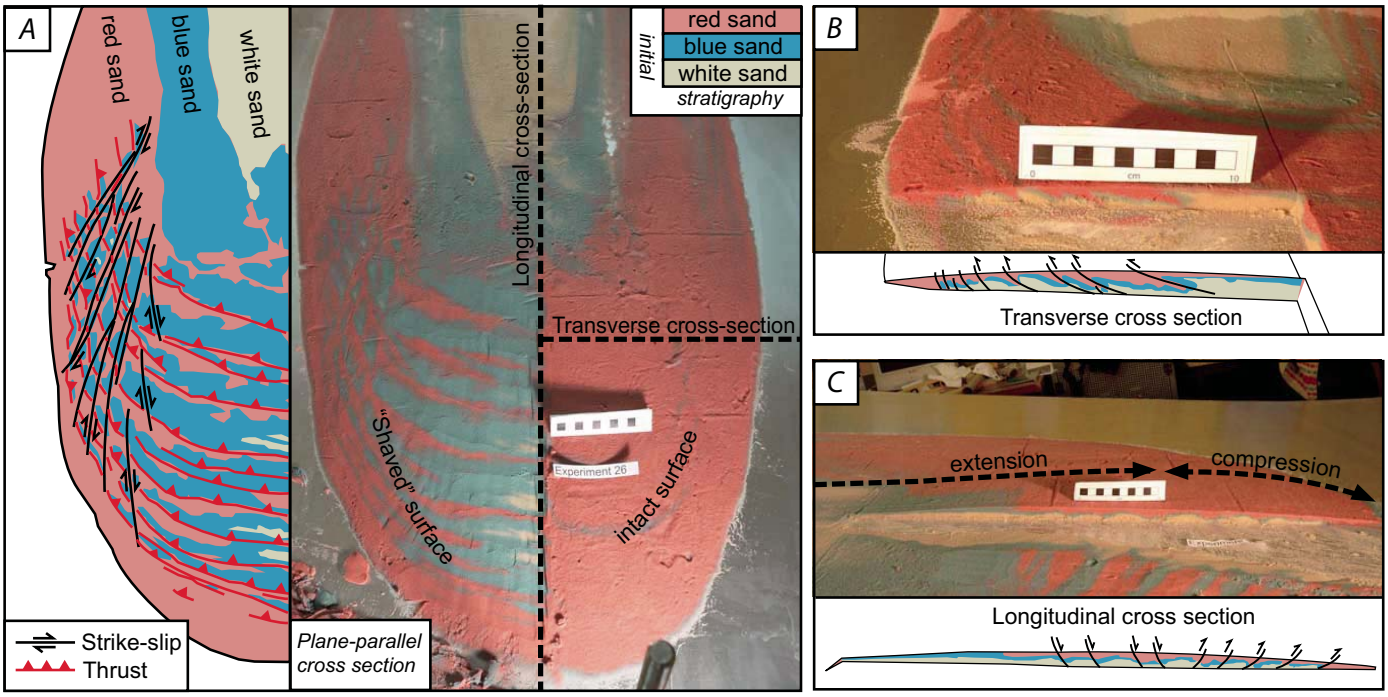

Figure 9. Cross sections from some scaled experiments. (A) Types of cross section with base-parallel cross section on left. Note that the lithological repetitions follow thrust-fault orientation. (B) Transverse and (C) longitudinal cross sections with preserved layering affected by various structures.

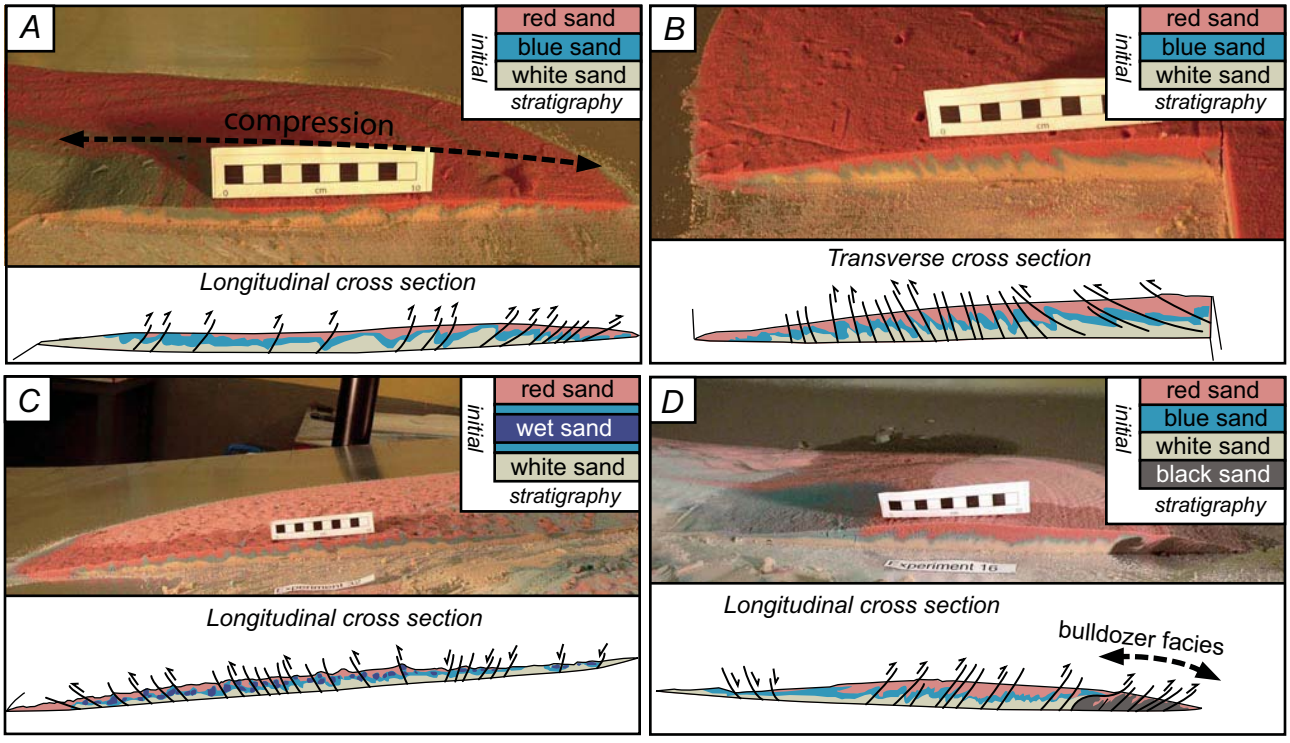

Figure 10. Various longitudinal and transverse cross sections from the experiments. (A) Longitudinal cross section of experiment 7 run on model 1 ramp, with layered colored sand; dominantly compressive structures are observed through the profile. (B) Transverse cross section of experiment 8 carried out on model 1 ramp; exclusively thrust faults appear. Note that the thrust-fault dip variations form center of mass to lateral margins. (C) Longitudinal cross section of experiment 32 run on model 2 ramp, where a humid sand layer placed between normal dry layers underwent boudinage processes and formed hummocks on the deposit surface. (D) Longitudinal cross section of experiment 16, model 1 ramp; the substratum layer (black sand) covering the sliding plane is entrained, accumulated, and piled up in frontal zones of the deposit.

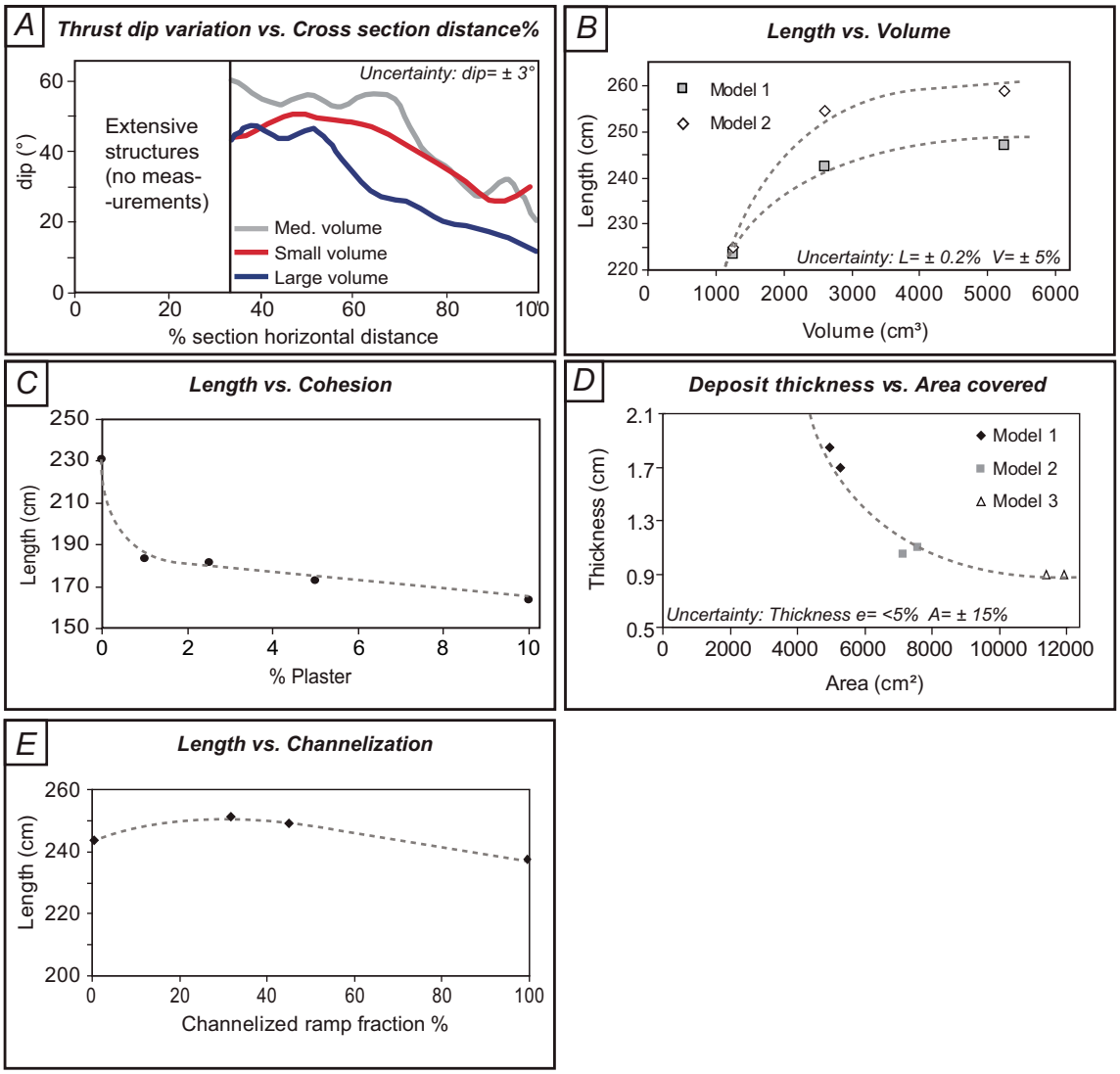

Figure 11. (A) Thrust faults dip variations in three deposits from model 1 ramp (corresponding to the three volumes) measured throughout longitudinal cross sections. X-axis represents the percentage of the distance from the beginning of the ramp curvature to the tip of the deposit. Measurements are only made for thrust faults since normal faults affect the thinner portions of the deposit, and are more difficult to characterize precisely. (B) Length versus volume graph for two of the three ramps (models 1 and 2) and for the three different volumes used in the experiments. (C) Length versus cohesion graph with cohesion expressed as plaster content ranging from 0% to 10%. (D) Effect of channelization on deposit length; *x*-axis refers to channelized percentage of the total sliding plane. The acceleration and deceleration planes are separated by a bar. (E) Deposit thickness versus area covered for the three ramp models. In a way, the relationship between area and thickness represents the spreading capacity of a mass. The arrow shows that the thinner the deposit and the greater area it covers, the greater the spreading capacity. For all plots, n is the total number of experiments, and the number of experiments used to average a given measurement are in parentheses.

surrounding valleys. Both scenarios were tested on model no. 1 by placing lateral walls separated by 32 cm. Measurements are subsequently expressed as a function of percentage of ramp channelized; accordingly, 100% represents a total confinement whereas 0% denotes an unconfined ramp (Fig. 11E). When the limiting walls were placed only on the acceleration plane (e.g., initiation plane), the resulting deposit thickness *e* was slightly lower (1.6 cm instead of 1.7 cm in standard unconfined experiments) and its width slightly decreased (52–53 cm instead of 55 cm). The distances reached did not show significant changes (247–249 cm instead of 242 cm); consequently, the *H*/*L* ratio stayed approximately equal. When the ramp was fully channelized (initiation plane and depositional plane), lateral levees were more abrupt and longer than in the standard experiment (Fig. 8E), the profile was still distally raised, and the front showed small digitations. Thickness stayed unmodified (1.65 cm) and the distance *L* was slightly lower (236 cm), though the deposit extended further back up the ramp. Structures were the same as in

previous experiments, but there were more strike-slip faults, especially toward the channel walls. Normal faults were still located at the back of the deposit and thrust faults in the frontal zones.

Effect of Topographic Obstacles

To characterize the effect of deflection by nearby topographic heterogeneities, one distal corner of the ramp was bent so as to form an oblique-to-flow valley wall. The resulting deposits (Fig. 8F) were asymmetric and the distances reached slightly lower than without a topographic obstacle (227.5–239 instead of 242 cm in the standard experiment), although deposit width and thickness were similar. The obstructed side of the deposit displayed a higher density of strike-slip structures and a higher lateral levee than the obstacle-free side; furthermore, a clear tongue-shaped subunit emerged from the obstructed side, traveling further than the rest of the mass. Striae or isolated ridges present on the initiation plane testified to the flow direction before deflection by the topography.

Presence of Mobile Substratum Material on Deceleration

To simulate dry substrata, a 3 mm layer of granular substratum (colored sand) was placed over the depositional plane. The obtained deposit (Fig. 8G) was emplaced only out to 205 cm (compared to 242 cm without substratum), was considerably thicker (2.3 cm compared to 1.7), and retained a similar width (53 cm compared to 55 cm). It was lobe shaped, well rounded, symmetric, and its lateral levees were prominent and wide. Two new families of conjugate ridges appeared on the deposit surface, with orientations varying between ±25°–45° relative to flow direction. The front had higher concentrations of thrust structures, which deformed not only the collapsed material, but also the underlying and entrained substratum. In cross section (Fig. 10D), the dip of thrust faults decreased toward distal zones; in particular, at the bulldozed substratum zones, the low dips were expressed on the surface by curved ridges pointing toward the front.

Ramp Curvature

Three different ramps were tested in order to determine the influence of the relationship initiation plane/depositional plane on the rockslide-avalanche features. Models no. 1–no. 3 had respective initial slopes of $\alpha = 45°$, 35°, and 30° and depositional slopes of $\beta = 0°$, 12°, and 18°, covering large curvature intervals. Accordingly, model no. 1 showed a stronger curvature (difference $\alpha - \beta = 45°$) than model 3 ($\alpha - \beta = 12°$). Figure 11D shows area *A* variations as a function of thickness *e*. In particular, when β rose close to the basal friction value of the aluminum pane, the sand was emplaced over a greater surface area and the deposit was thinner. Figures 8A, 8H, and 8I show standard experiments for ramps 1, 2, and 3; while model no. 1 generated lobed ovals, those of no. 2 are more elongated, and those of no. 3 are tongue shaped. In all cases the same types of structures appeared; only their concentration and distribution varied. Accordingly, the ramp with higher curvature (i.e., no. 1) had deposits affected by higher densities of thrust faults toward the front than the no. 2 and no. 3 model ramps. Models 2 and 3 showed higher concentrations of normal faults toward the back and center of the deposit. Increases in curvature also were positively correlated with lateral strike-slip fault intensity. In cross section, all deposits generated by the no. 1 ramp showed distally raised profiles while those produced by no. 3 had uniform profiles. In turn, the no. 2 ramp formed intermediate profiles, slightly raised distally.

Deformation and Velocity Evolution

Surface deformation and velocity data were acquired by video cameras. The major portion of the 2600 cm^3 box was filled with white sand, while the uppermost 0.5 cm had four colored equal-area rectangles that served as markers to follow deformation and variations in rockslide-avalanche shape. Figure 12 and Animations 1 and 2 illustrate the evolution of these 4 surfaces during the 2.40 s of transport, subdivided into 0.08 s intervals. Velocity was measured at the front, center, and back of the moving mass. The front accelerated earlier than the back of the mass, which reached similar velocities later. The average calculated velocity is ~1 m s^{-1} for model 1, 0.85 m s^{-1} for model 2, and 0.5 m s^{-1} for model 3. In Figure 12, the four zones

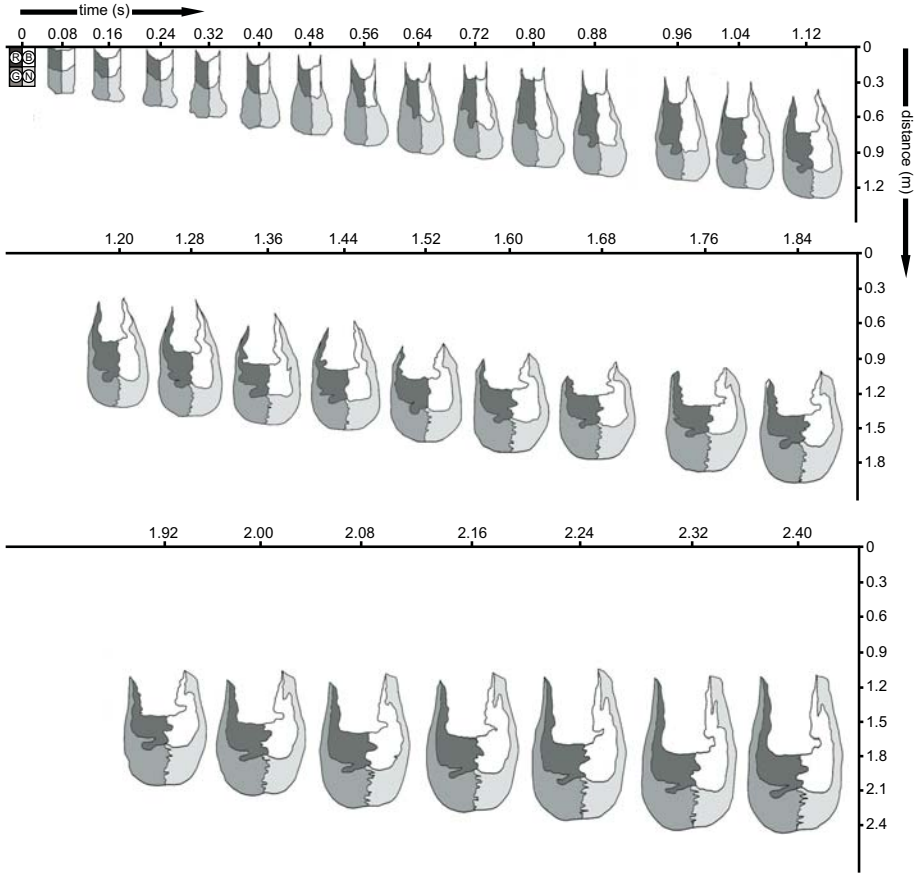

Figure 12. Deformation stages in the moving granular scaled rockslide avalanche measured through video images. The X-axis shows total elapsed time (0.08 s intervals) and the Y-axis shows the distance reached. The initial material was covered by a fine (3–4 mm) layer of various colors of sand separated in four equal-area rectangles. This allowed following surface deformation throughout the flow.

Animation 1. Video sequence of one of the analogue experiments involving a thin colored sand surface with four equal areas of distinct colors above a uniform white sand layer. These types of experiments were used to characterize deformation during motion and emplacement. To view the animation, you will need Windows Media Player or a multimedia player such as Real Player. If you are viewing the PDF of this paper or reading it offline, please visit http://dx.doi.org/10.1130/GES00131.SA1 (Animation 1) or the full-text article on www.gsajournals.org to view Animation 1.

Animation 2. Close-up of Animation 1. The late-forming strike-slip faults can be easily seen just before movement completely ceases. To view the animation, you will need Windows Media Player or a multimedia player such as Real Player. If you are viewing the PDF of this paper or reading it offline, please visit http://dx.doi.org/10.1130/GES00131.SA2 (Animation 2) or the full-text article on www.gsajournals.org to view Animation 2.

preserve good lateral symmetry through time; the front is strongly stretched during the first phase then gradually joined by the back area, which in turn undergoes strong stretching. A certain fraction decelerates on the sides, forming the lateral levees. Then the front enters a compressional stage and tends to spread laterally while undergoing longitudinal shortening. Velocities at the center of the mass are always higher than at the edges.

The measured velocities allow us to calculate bulk strain rates of $\sim\dot{\varepsilon} \approx 3\ s^{-1}$ in our experiments. This is calculated using a strain of ~9 (20 cm is stretched to 200 cm) in an emplacement of ~3 s. Typically maximum strain rates in nature are $\sim\dot{\varepsilon} \approx 6 \times 10^{-2}\ s^{-1}$, taking a maximum strain of ~19 (1 km stretched into 20 km) and a rapid emplacement of 300 s. Thus, strain rates are higher in models than nature. The strain rate over individual structures, rather than the deposit as a whole in both models and nature, would be much less than the bulk strain rate. As long as the material stays in the frictional regime, both analogue and natural examples will form Mohr-Coulomb faults that are rate insensitive.

INTERPRETATION

Structures

We review the recurrent structures that appear in our experiments. Thrust faults are the most ubiquitous, and testify to the compression affecting the frontal and some central regions of the mass. In certain experiments they are perpendicular to flow direction, in others they are curved, pointing toward the front and with a tendency to parallel the general transport direction at the lateral margins of the deposit. They are seen to form early, as soon as the mass leaves the acceleration plane for the deceleration plane. This early formation is illustrated on video by the appearance of lithological repetitions in frontal zones, aligned with thrust structures. The front of the mass slows down first and produces a ramp effect, where material behind accumulates and shoves the front forward.

The thrust faults are frequently crosscut by strike-slip fault systems, generally subparallel to transport (±15°–20°). Consequently, the latter appear to form after the majority of thrust faults; however, some are seen to develop alongside the thrusts, as lateral ramp structures or relay faults. The velocity variations causing strike-slip faulting can be created by slide surface heterogeneities or by intrinsic differences (e.g., layer thickness, grain size). They initially form parallel to flow, but are subsequently moved toward lateral edges as the bulk of the mass moves forward. During rotation they also acquire a partial thrust component. In addition, early-formed thrust faults are rotated at the edge and develop strike-slip motion.

Normal faults generally materialize at the back of the model. They are not perfectly linear, but their orientation stays perpendicular to flow direction. They seem to form when the granular mass stretches in the first phase of the collapse, and they are progressively converted or replaced by thrust faults as the compression generated at the front during deceleration is able to propagate sufficiently far back.

Volume

As in nature, the laboratory experiments show that an increase in initial material volume results in an *H*/*L* decrease; however, the range covered does not allow definitive interpretation. Superficial structures remain identical in location and orientation when increasing the initial collapse volume; only their concentration increases. This observation supports our scaling: scale reduction only has an effect on structure density and not on their nature and position.

Cohesion

Adding plaster in the granular mixture increases overall cohesion, and tends to prematurely stop the moving mass while favoring the formation of compressive structures over extensive structures. A very small percentage is sufficient to greatly modify the behavior of the experiment. By analogy, we can assume two phenomena are opposed in nature: the formation of fine materials by fragmentation processes should theoretically increase cohesion and thus reduce mobility. In most examples this does not seem to be the case. We must therefore imagine that this fine rock powder is maintained, at least at the base, in a fluidized or liquidized state during a certain period. In turn, in the bulk part of the rock mass, fine material may well increase cohesion and favor brittle behavior, akin to the experimental rockslide avalanches.

If one, or several, cohesive layers (plaster or humid sand) are sandwiched between normal sandy sequences, brittle domains separate from each other and form hummocky topographies on the deposit. This observation is crucial in that it shows a single deposit could readily contain evidence of extension (hummocks) associated with compressive structures (thrust faults).

Confinement

When the granular slide is partially canalized on the acceleration plane, the mass spreads normally as soon as it leaves the valley walls. This confirms that a moving rock mass will initiate its spreading phase in the reduced-slope depositional surface rather than on the high-slope acceleration plane. In addition, the deposit reaches similar distances to its unconfined version. Hence, partial channel confinement

parallel to slope direction on the acceleration plane does not significantly modify the slide *H*/*L* ratio. When the slide is completely canalized by slope-parallel valley walls, its runout also remains comparable. Shaller (1991) reached a similar conclusion concerning canalized runouts. On the other hand, confinement by valley walls has a strong effect on lateral structure formation. Strike-slip structures are accentuated toward both sides, and lateral levees are longer, more abrupt, and better marked in the topography.

Sliding Plane Heterogeneities

When significant sliding plane topographical variations are present on one side of the flow path, these tend to deflect the mass and provoke the formation of tongue-shaped subunits in frontal regions. These subunits are bordered by long strike-slip structures that accommodate velocity differences created by the deflection. The opposite side of the mass is able to spread freely, even if it was deflected.

Dry Substratum on Deceleration Plane

When the depositional surface is covered by a dry, unconsolidated, granular substratum, the slide is slowed. The substratum is rapidly pushed and accumulated at frontal regions of the moving mass, absorbing and dissipating kinetic energy, thus acting as a brake. New families of contraction-generated surface ridges formed because the mass was unable to spread freely. Note that the substratum used here was only on the depositional plane, thus these results can simulate only structures in the frictional regime. Rockslide avalanches are known to incorporate material, possibly increasing the runout, and this incorporation occurs in the fluidized basal shear zone (e.g., Hungr and Evans, 2004; Bernard et al., 2008). This process has not been modeled here. The structures generated here are more akin to the bulldozed facies of the rockslide-avalanche front (Belousov et al., 1999).

Slide Plane Curvature

When the depositional slope is high (e.g., when it approaches the basal friction angle), the area covered by the deposit is greater and its thickness is reduced compared to the standard experiment. Thus, spreading capacity is positively correlated with depositional slope increase. Model 1 experiments form oval-shaped deposits, while model 2 deposits are more elongated, and model 3 deposits are tongue shaped. As a consequence, there is a simple correlation between slide deposit shapes and the initiation-depositional plane relationship (ramp curvature). Furthermore, proximal normal fault cover and lateral strike-slip density both increase at lower curvature (e.g., model 3). In cross sections, model 1 deposits show distally raised profiles, whereas those produced by model 3 have uniform, homogeneous profiles. Model 2 deposits form intermediate profiles.

Kinematics

Velocity variation studies demonstrate that upon release, the front of the granular flow accelerates earlier than the back (i.e., the latter reaches similar velocities thereafter). Average calculated velocity is 1 m s^{-1} for model 1, 0.85 m s^{-1} for model 2, and 0.5 m s^{-1} for model 3. Possibly the average slide velocity is positively correlated with an increase in initiation plane slope. A detailed time analysis of the evolution of deformation affecting the moving mass (Fig. 12) allows us to propose the following general kinematic model.

1. Movement initiates from the front, which undergoes extension with intensity depending on initial slope (i.e., higher initial slope results in a longer and more intense extension period). The back starts moving later.
2. The whole mass is in movement; flow velocities between the front and the back are now comparable.
3. Spreading first occurs at the front of the mass, as this is the zone that first reaches the depositional plane. Velocities are always higher at the center of the mass than at lateral margins.
4. During motion, the material at the front is pushed sideways and forms primary lateral levees. These levees still are in motion and are progressively modified as the mass continues its trajectory.
5. Frontal velocity starts to decrease; the first compressive structures form while velocity at the back is still maximal and extension still affects these regions. The central part of the mass still pushes the material sideways and provokes the formation of sets of strike-slip faults near lateral levees.
6. While the front still moves forward, frontal compression propagates toward the back of the mass (ramp effect), and the central part slows down. During this phase, long strike-slip faults appear in various zones to accommodate relative velocity differences already present throughout the flow.
7. When kinetic energy is insufficient at the front to prevail over frictional forces, the mass stops. The last compressive and strike-slip structures appear where still mobile portions are blocked by immobile regions.
8. During the stopping phase, numerous small strike-slip faults form and crosscut the majority of thrust structures with small displacements.

MODEL VALIDITY

In this section we investigate the analogy of the internal structures, kinematics, and dynamics of our models to natural rockslide avalanches.

Dynamic and Geometric Similarity

Figure 13 illustrates various relations between the previously defined Π numbers.

Dimensionless initial energy Π_6 versus dimensionless runout Π_4

Data follow a diffuse trend, and for each environment (extraterrestrial, volcanic, non-volcanic, and experiments) we can outline individual tendencies. The experiments plot on the general trend confirming the validity of measured runout lengths for such fall heights, considering the small volumes used. (See Fig. 13A; n = 234 with 187 natural examples and 47 experiments.)

Dimensionless volume $\Pi_{6'}$ versus dimensionless area Π_7

Generally the data define a relatively well constrained trend with positive slope. The power law regression line shows a good R^2 = 0.76. Experimental data are included in this trend, toward the lower values. Therefore there is a good geometrical similarity between the analogue models and nature in terms of area covered by the deposits for a given collapse volume. We calculate an equation in the form

$$\Pi_7 = 15\Pi_{6'}^{\frac{2}{3}}, \qquad (6)$$

which strongly resembles the area and volume relationship described by Dade and Huppert (1998) and Kilburn and Sorensen (1998); their equations apply to Bingham type materials, and just like these authors we find it difficult to explain why such a relation applies to granular materials in our frictional model. (See Fig. 13B; n = 157 with 47 experiments and 110 natural deposits.)

Structural and Morphological Similarity

Shape

Laboratory deposits show three distinct shapes (lobe shaped, irregular, and tongue shaped) out of the four possible, which furthermore depend on the initiation versus depositional plane ratio, surface obstacles, and confinement. Fan-shaped

deposits such as Ollagüe (Fig. 4E), Tetivicha (Fig. 5A), and the northeastern margin of Llullaillaco (Fig. 5B) are not obtained in our models. Tongue-shaped deposits comparable to Aucanquilcha (Fig. 4C), to the northeastern subunit of Socompa (Fig. 1), and the southeastern extremity of Llullaillaco (Fig. 5B) can be reproduced in our experiments with integral channelization of the rockslide avalanches, or with a model 3 type ramp with relatively low initiation planes (~30°) and relatively high depositional surfaces (18° in model 3). Tongue-shaped subunits also develop in the laboratory when the mass is deflected by topographical obstacles (Fig. 8F). The lobe-shaped deposits are probably the most common both in the models and in natural examples.

Profile

Experiments successfully reproduced three out of the four types of profiles observed in natural deposits: i.e., distally raised, uniform, and irregular profiles. Proximally raised profiles are never obtained in analogue deposits, and in nature these seem to characterize deposits with a significant proportion of slump and/or torneva blocks such as Parinacota (Fig. 5C). These deposits may be formed by retrogressive failure not modeled here. Uniform profiles are observed at Mombacho South (Fig. 2C), Chaos Jumbles (Fig. 2B), Aucanquilcha (Fig. 4C), Llullaillaco (Fig. 5B), the eastern side of Socompa (Fig. 1), Lastarria (Fig. 4D), and inferred for Olympus Mons landslides on Mars (Fig. 5D). In laboratory experiments, uniform profiles are achieved for deposits that have fewer compressive structures, on ramps with relatively steep depositional planes (e.g., model 3). Distally raised profiles occur at Mombacho North (Fig. 2C), Ollagüe (Fig. 4E), at the western side of Socompa (Fig. 1), and at Blackhawk (Fig. 2A). These are reproduced in the majority of our experiments associated with high concentrations of compressive structures, when a model 1–type ramp with a high initiation slope and a low depositional slope is used. In these, compression provokes piling-up of the material, thus adding thickness to distal zones.

Confinement

Deposits resulting from deflected, lightly or heavily confined rockslide avalanches tend to show a higher variability and density of surface structures than unconfined equivalents. The Carlson (Fig. 4A) deposit and both Llullaillaco northern and southern deflected subunits (Fig. 5B) display a higher concentration in longitudinal ridges at lateral margins, just as in our granular canalized experiments (Fig. 8E). Deflected rockslide avalanches often form accumulation levees and/or strike-slip fault–rich zones (e.g., northeastern zone of Chaos Jumbles, Fig. 2B; eastern zone of Martinez mountain, Fig. 4B; northern side of Parinacota, Fig. 5C; frontal levees at Socompa, Fig. 1), very similar to those illustrated by analogue models when a portion of the sliding surface is obstructed (Fig. 8F).

Deposit characteristics

Natural and analogue model deposits share the following morphological and structural aspects.

1. Preserved gross stratigraphy (all color-layered experiments, Mombacho North and South, Ollagüe, Socompa).
2. Incorporation of substratum by bulldozing (experiment in Fig. 8G and cross-section Fig. 10D, Carlson, Blackhawk, Mombacho

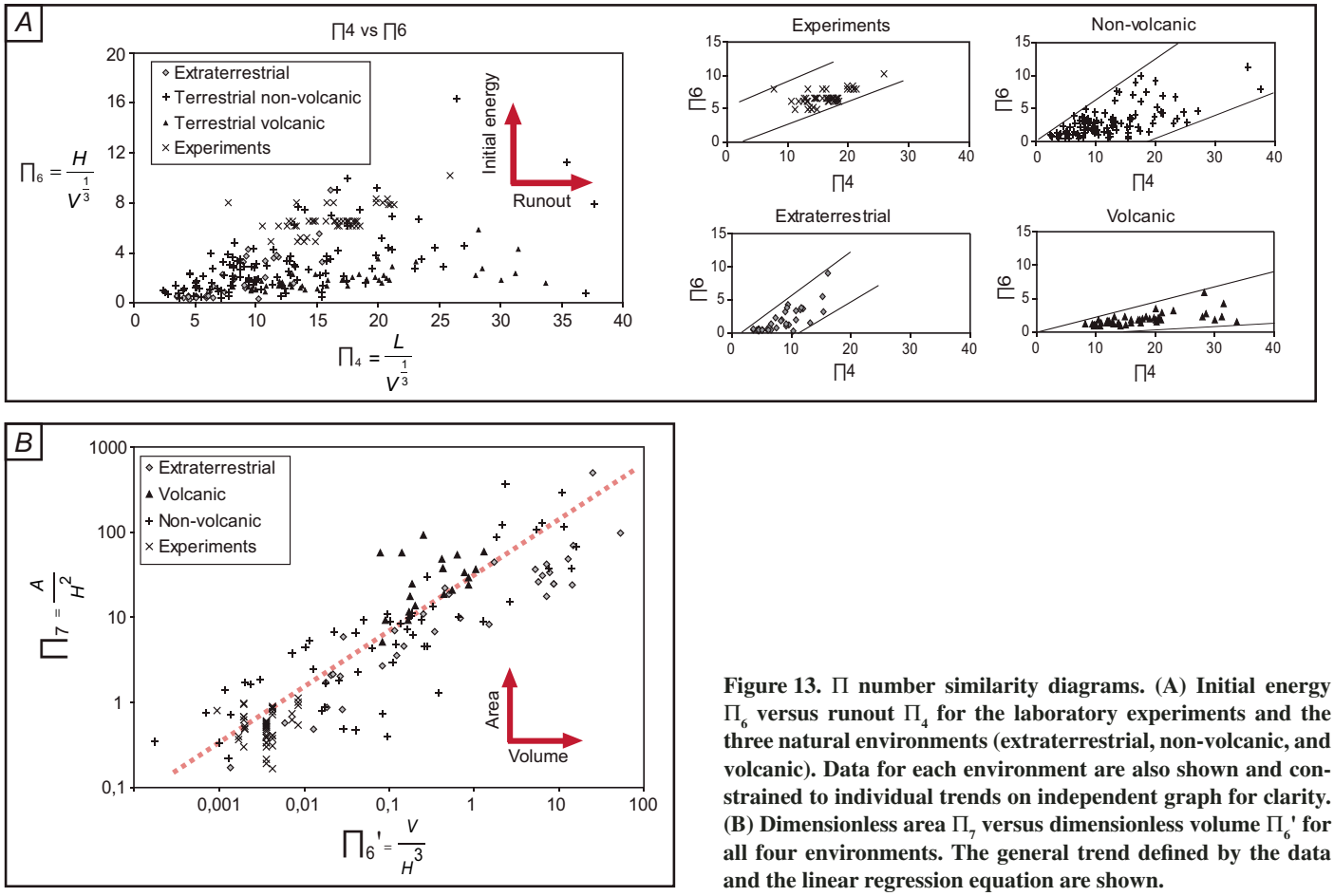

Figure 13. Π number similarity diagrams. (A) Initial energy Π_6 versus runout Π_4 for the laboratory experiments and the three natural environments (extraterrestrial, non-volcanic, and volcanic). Data for each environment are also shown and constrained to individual trends on independent graph for clarity. (B) Dimensionless area Π_7 versus dimensionless volume Π_6' for all four environments. The general trend defined by the data and the linear regression equation are shown.

North, Ollagüe, Tetivicha, Llullaillaco, Parinacota, and Socompa).
3. Presence of initiation and/or failure plane striations (experiments in Figs. 8D, 8F, 8G; Chaos Jumbles, Lastarria, Mombacho North, and Tetivicha).
4. Vertical recurrence of lithologies (color-layered experiments, models 1 and 2; Aucanquilcha, Socompa, Llullaillaco) associated with thrust structures (central to distal transverse ridges seen in regions of all experiments; Chaos Jumbles, Carlson, Martinez Mountain, Blackhawk, Lastarria, Aucanquilcha, Ollagüe, Tetivicha, Llullaillaco, Parinacota, Socompa, and Olympus Mons).
5. Strike-slip structures and longitudinal ridges (all experiments and all natural deposits except at Mombacho where hummocky topographies hide most existing longitudinal ridges).
6. Hummocky surfaces (Figs. 8C and 8D; Mombacho North and South, Parinacota, Ollagüe, Llullaillaco, Tetivicha).
7. Oblique ridges (toward lateral margins in all experiments; Chaos Jumbles, Martinez Mountain, Aucanquilcha, Lastarria, Llullaillaco, Socompa).
8. Lateral levees (most experiments; Carlson, Martinez Mountain, Blackhawk, Lastarria, Llullaillaco, Socompa).

The analogue model partially succeeds in reproducing normal faults and/or proximal transverse ridges; always in proximal regions in the experiments, located in various regions in nature. It also crudely reproduces gross inverse grading when hummocky topography is generated and fine particles tend to gather between and under large analogue block portions (e.g., cross section, Fig. 10C).

IMPLICATIONS OF MODEL AND NATURAL STRUCTURES

Ridged or Hummocky Surface?

Our experiments show that dominantly fine-grained and homogeneous granular material slides tend to generate deposits with well-marked superficial structures (dominantly ridged) comparable to those of Lastarria, southern Llullaillaco, and Aucanquilcha. Even though its initial material was heterogeneous in size and type, Socompa could also be included in this category, knowing that the fine substratum portion of the deposit actually makes up 90% of the total volume (van Wyk de Vries et al., 2001); thus its behavior was probably dominated by the latter finer material and formed ridge structures on the deposit topography. On the other hand, the analogue model demonstrated that collapses composed of initially heterogeneous materials (e.g., the alternation between scoria layers and lava flow units in volcanic environments, the different lithologies in mountain chains, and the plaster and/or sand alternation in the experiments) tend to generate hummocky surfaces like those at Mombacho, Parinacota, Ollagüe, and Tetivicha. The latter are likely to obscure the possibly existing ridged structures.

Bulldozer Structures

Experiments also showed that emplacement of a rockslide avalanche on a dry, unconsolidated substratum in the depositional area, creates bulldozer structures in its frontal regions similar to those described at Shiveluch by Belousov et al. (1999). Other natural examples fit this model, such as Blackhawk, Llullaillaco (fine pyroclastic deposits acting as substratum under the southern subunit were pushed and accumulated at the front; J.E. Clavero, 2006, personal commun.), Ollagüe (salar deposits; Clavero et al., 2005), and Tetivicha (salar deposits). At Sherman (Shreve, 1966), large amounts of blocks of ice and snow from the underlying glacier were bulldozed by the traveling rock mass. Particular care must nevertheless be taken to avoid confusing substratum entrained and bulldozed during the flow, and substratum involved in the initial failure (e.g., Socompa, van Wyk de Vries et al., 2001; Mombacho, Shea et al., 2007). Note that we did not model entrainment of a water-saturated substrate (because of capillary cohesion issues at the laboratory scale), which is thought to undergo liquefaction effects and enhance mobility (Hungr and Evans, 2004). We did not model substrata erosion and incorporation on the acceleration plane that may also induce bulking (e.g., Bernard et al., 2008).

Ramp structures and deposit profiles

In our scaled model, when the depositional slope decreases, compressive structures increase and propagate toward the center of the deposit, resulting in a frontal ramp effect. This piling up of materials differs significantly from the bulldozer structures described here and is more similar to the structures described by Shreve (1968) at Blackhawk. The bulldozer effect derives from the ripping off, transport, and marginal accumulation of unconsolidated or fragmented substratum during final deceleration, whereas the ramp effect corresponds to internal imbricate layers in frontal portions of the mass generated by thrust faults during the deceleration phase. In both cases, fault dip tends to decrease toward the deposit front. Accordingly, natural avalanche deposits may have distally raised profiles due to ramp and/or bulldozer structures, which in turn could derive from low depositional slopes (i.e., 0° in model 1) associated with relatively high acceleration slopes (i.e., 45° in model 1). This is effectively the case at Mombacho North, Ollagüe, and Blackhawk. Their profiles are all, to some extent, distally raised, and their initial acceleration planes have high slopes compared to their deceleration plane. In contrast, experiments show that relatively high-slope depositional planes (i.e., 18° in model 3) associated with relatively low acceleration planes (i.e., 30° in model 3) tend to generate uniform profiles. This observation is verified at Lastarria, Aucanquilcha, Chaos Jumbles, and Llullaillaco, where depositional planes have higher slopes than at most other sites. The situation is somewhat different at Socompa, where a uniform profile dominates the eastern regions (5°–10° depositional slope) and a raised profile dominates the northwestern areas (slope opposed to flow direction).

Strong Relationship Between Deposit Shape and Surrounding Topography

When our scaled models are neither confined or canalized, and are carried out on a low deceleration slope coupled with a high acceleration slope (i.e., model 1), the resulting deposits are well spread laterally and have lobate spoon shapes comparable to those of Mombacho North and South, Tetivicha, Ollagüe, and Olympus Mons deposits. The inverse situation, relatively low acceleration slope and/or relatively high deceleration slope (i.e., model 3), produces tongue-shaped deposits similar to Aucanquilcha, Lastarria, Chaos Jumbles, and Martinez Mountain. The only notable exception to this is Blackhawk, which has an elongated shape, even though its initial slope is high and its depositional slope low. The difference between lobe-shaped and/or spoon-shaped and fan-shaped deposits could arise from general dynamics of the rock mass during its emplacement: a mass decelerating strongly at its front could produce a lobe aspect, whereas a mass completely free to spread in most directions and not slowed down by its front would produce a fan-shaped aspect, as suggested by Shreve (1966) for the Sherman landslide. Unfortunately our experiments are not able to confirm this hypothesis, perhaps because of insufficient kinetic energy when our granular flow approaches the depositional plane or simply because basal friction is still too high compared to natural large-scale landslides. Irregular shapes such as those at Parinacota or Carlson deposits are provoked by strong confinement or channelization. The Carlson rockslide was fully canalized in a 300-m-wide by ~1-km-long

valley and was only able to spread after leaving the valley walls. At Parinacota, the northern area is obstructed by high topographic barriers whereas the southern regions allowed the mass to advance with only slight confinement. At Ollagüe, the southern zone that entered the Salar de Carcote reached lower distances than the northern deposit that spread outside the salar (salt flat). The salar is quite unconsolidated, and probably absorbed kinetic energy from the arriving mass, in a similar fashion to our experiments when granular substratum was on top of the sliding surface. Water is probably another medium that opposes free spreading by absorbing significant kinetic energy. The Mombacho North deposit (Las Isletas) entered Lake Nicaragua and was possibly slowed down in this way. At Socompa, eastern hills provoked the deflection of the moving mass to the northeast, which probably produced the median scarp described by Francis et al. (1985), Wadge et al. (1995), and van Wyk de Vries et al. (2001).

Structural Genesis

Our kinematic characterization shows that the front of the slide stops prior to its center, but after the back, which agrees with observations made by Shreve (1968), but only partly agrees with the numerical model of Kelfoun and Druitt (2005), where the mass freezes first in its proximal then at its distal zones. The difference may be related to their dominantly compressive or dominantly extensional affinities. In our experiments, extension initially affects the mass, and is later replaced by compression, which indicates that normal faults could be converted into thrust faults. This strong connection between the two explains the possibility of observing compressive features associated with boudinage structures in the same deposit. Lateral velocity variations throughout the mass are probably responsible for the formation of strike-slip faults, two different families of which can be distinguished: large, infrequent, early strike-slip structures, from late, smaller but abundant strike-slip faults. In all cases, the video images show that many structures form early during flow and not just during the stopping phase. Figure 14 summarizes the progression of structure formation inferred from our models.

Is Superficial Morphology Representative of Internal Structures?

Transverse surface ridges formed in our experiments do not share the same spacing when compared to internal thrusts from the interior of the deposit. Most likely, surface granular rearrangements take place progressively as the mass slides, preventing the formation of high amplitude–long-wavelength structures. This observation is less valid when focusing on transport-parallel structures such as strike-slip faults, which only form thin, low-amplitude discontinuities on top of and within the deposit. The question still arises, do superficial structures in natural rockslide-avalanche deposits represent internal structures formed during flow, or surface waves? From our experiments, we deduce that a majority of early forming strike-slip faults are preserved after runout; nevertheless, transverse structures (normal and thrust faults) mostly represent the last deformation phases in the regions where they appear.

Active Levees

Analogue model lateral levees appear either when material is deposited and pushed aside by moving material at the front (unconfined rockslide avalanches), or when the mass is canalized, in which case the levees are more abrupt and bounded by numerous strike-slip faults. In nature, levees at Blackhawk, Carlson, Martinez Mountain, Lastarria, Llullaillaco, and Socompa are generally associated with confining environments. Channelization or confinement, whether in nature or in the models, tend to increase longitudinal ridge and/or strike-slip structure density, particularly near the margins. On the other hand, natural unconfined deposits do not show levees akin to our experiments. Consequently, rockslide-avalanche levees could differ significantly from dense pyroclastic flows or lava flows in the dynamics of their formation. Where the later levees are usually thought to represent a recording of the highest thickness reached by the flow in zones that become stationary, they are associated in our case to in-motion processes and lateral push. They are modified as the mass progresses forward, and the oblique ridges near them observed on the video form to accommodate the lateral push.

Two Morphological and Two Dynamic Types of Rockslide Avalanches

From the above interpretations, and as a general summary, we can separate rockslide avalanches into two textural categories, hummocky and ridged, and two dynamic types, dominantly extensional and dominantly compressive rockslide avalanches. Figure 15A illustrates the formation of these two pairings (type 1—dynamic pole 1 and morphological pole 1; type 2—dynamic pole 2 and morphological pole 1; type 3—dynamic pole 2 and morphological pole 2; type 4—dynamic pole 2 and morphological pole 2). Generally, a collapse occurring on a highly curved sliding surface will form a laterally well spread, distally raised deposit with mostly compressive structures (type 1), whereas one occurring on a moderately curved sliding surface will display a laterally restrained uniform deposit affected dominantly by extension (type 2). The major difference between these dynamic poles is in the propagation of compression during the slide stopping phase. Thus at Mombacho South, Ollagüe, Tetivicha, Socompa, Llullaillaco, and Aucanquilcha, compression is concentrated in frontal zones and did not propagate backward. In contrast, at Blackhawk, Chaos Jumbles, Carlson, and Martinez Mountain, compression affects a great fraction of the deposit from front often up to central zones.

Furthermore, collapses composed of heterogeneously sized and/or heterogeneously competent material will generate a deposit

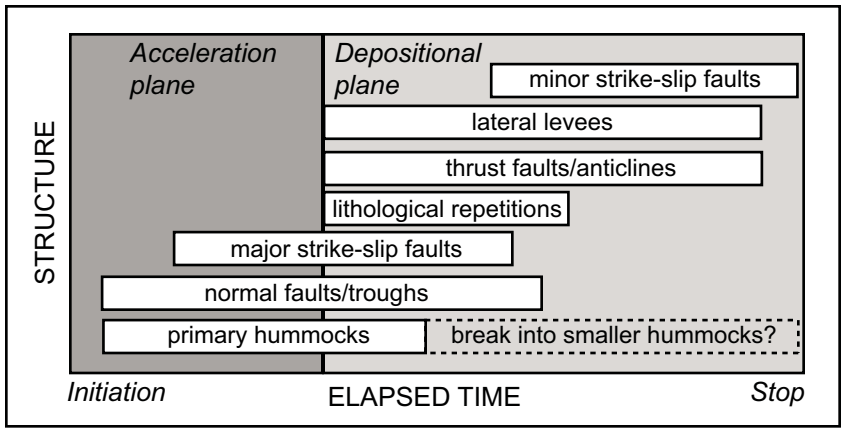

Figure 14. Summarized diagram of structure genesis in laboratory scaled rockslide avalanches during flow. The X-axis represents the transport time line, from initiation to stoppage, and the Y-axis simply separates distinct structure types. The bar represents the limit between the acceleration plane and the deceleration plane.

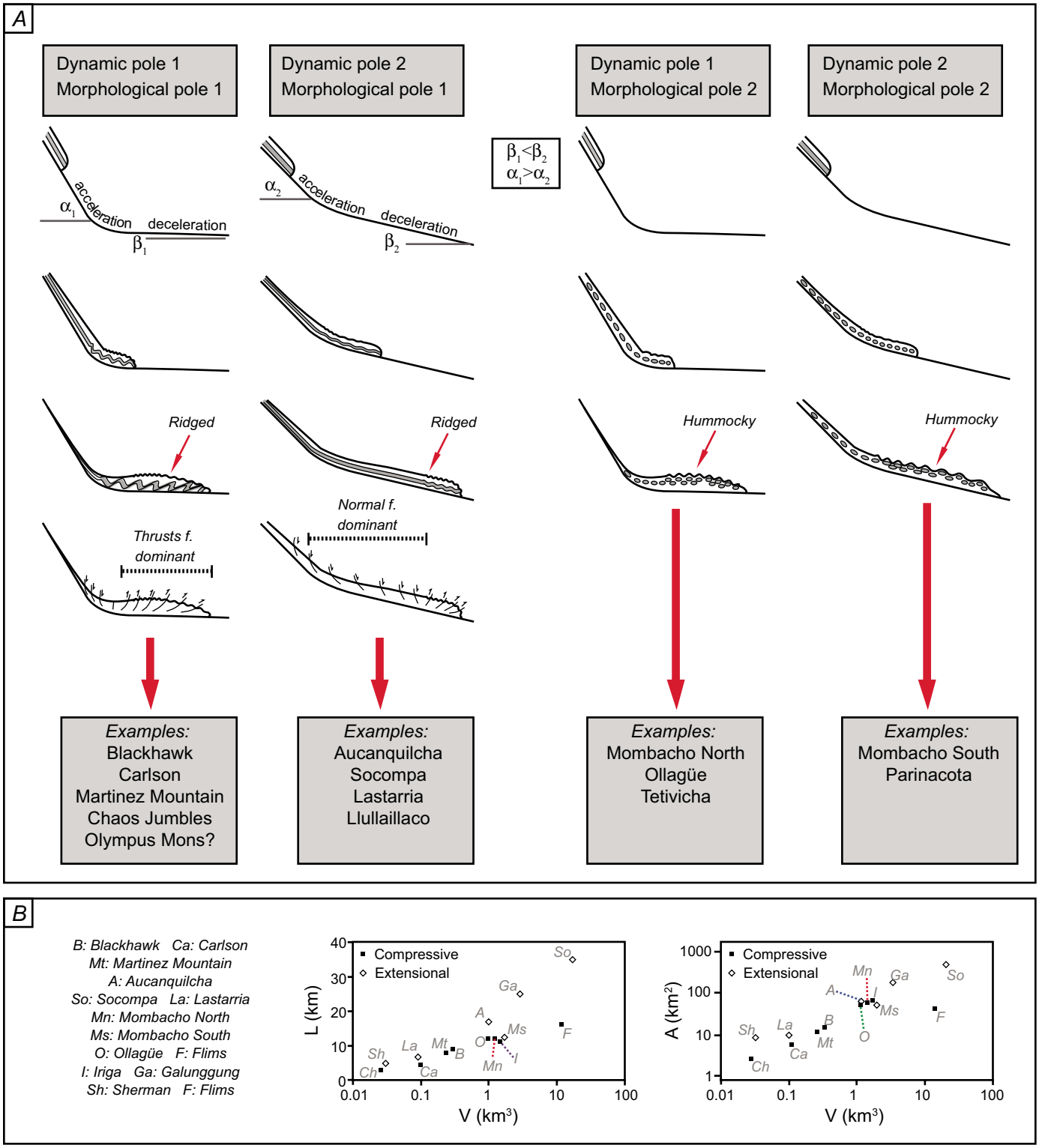

Figure 15. (A) Formation of the two morphological types of rockslide avalanches (hummocky and ridged) and the two dynamic types (extensional and compressive) with typical associated structures and their natural occurrences. (B) (*L*) Length versus volume (*V*) and area (*A*) versus volume plots (in both cases *V* axis is in logarithmic scale). Some of the studied rockslide avalanches (Parinacota, Tetivicha, Olympus Mons, and Llullaillaco) were not plotted due to insufficient data. Instead, some other known natural examples not detailed in this study (Galunggung, Sherman, Flims, and Iriga) were taken as additional data points because their extensional or compressive natures are more conspicuous. Just like the other rockslide avalanches, they were the objects of structural and geometrical analysis before being classified into their categories. Note that except for Mombacho South in both graphs, all compressive rockslide avalanches are below their extensional homologues, meaning that they reach shorter distances and cover smaller areas.

showing a hummocky, ridge-poor and structure-poor topography (types 3 and 4), whereas collapses composed of homogeneously sized and/or homogeneously competent rock fractions tend to display a hummock-poor, ridged, and structure-rich surface on their deposit (types 1 and 2). Our hypothesis of hummock formation consequently differs from that proposed by Clavero et al. (2002) and Clavero et al. (2005) for Parinacota and Ollagüe, respectively, which suggests that they derive from zones originally separated by faults and not from differences in material sizes and cohesion and/or lithology. Hummocks do not appear on monolithologic deposits; hence a minimum cohesion difference must exist within initial material. Certain factors may influence these major groups, such as the presence of an unconsolidated or competent substratum or even surrounding topography (mountains, valleys, and plains).

The validity of our approach can be summarized onto length versus volume and area versus volume plots (Fig. 15B), where we separate a certain number of the studied rockslide avalanches according to their structural type: dominantly extensional or dominantly compressive (see Supplemental Table 2[3]). Unfortunately, in some cases (Parinacota, Tetivicha, Olympus Mons, and Llullaillaco) data are insufficient for plotting, so we added some deposits not described in detail in this paper (Flims, Sherman, Galunggung, and Iriga) for which the data are available. Similar to the described avalanche deposits, a structural analysis and classification were made for these avalanches following the same method. Length alone was chosen instead of the *H*/*L* coefficient for plotting due to the identical meaning it provides, but with less scatter (Legros, 2002). The resulting graphs show that in both cases almost all compressive data are located below extensional data (except for Mombacho South). This confirms that for the same volume, a compressive rockslide avalanche will tend to reach lesser distances and cover smaller areas than extensional rockslide avalanches.

CONCLUSIONS

Natural rockslide avalanches are full of fault structures that can be successfully reproduced using a sand-based granular slide model. Any model of rockslide-avalanche kinematics or dynamics must take such structures into account, and the analogue models provide a useful way of exploring their development and significance. The models reproduce all structural features seen in natural examples, and the runout in the experiments is similar to that of natural small-volume events. However, because of the different balance between driving force and friction in the model (which is too high), the rockslides stop earlier in the models than many volcanic examples. Even so, model parameters such as dimensionless volume and dimensionless surface area show relationships similar to those found in Dade and Huppert (1998) and Kilburn and Sørensen (1998).

The structures form from the initiation of the slide, as the material is released. Normal faulting is developed first as the slide extends. Thrusts are produced when the front area starts to decelerate more than the back of the slide. Differential movements then create strike-slip faults that remain active until the slide halts. Final deposit surfaces can be grouped into two textural types, hummocky or ridged. The hummocky textures are produced by differences in the cohesion of the initial layering. Ridged textures are produced when the initial material is homogeneous.

The structures in the final deposits can also be grouped into two kinematic types, compressional or extensional. The limit between the two is controlled by the topographic profile of the slide. If it goes from steep to flat, then the regime is compressional; if the profile is more regular, then extension dominates. Primary results deduced from our classification showed that natural compressional rockslide avalanches have lower runout and cover a smaller area than their extensional equivalent at similar volumes.

Our analysis shows that a brittle plug flow model or basal slide-dominated model fits well with both natural and model rockslide avalanches. Mixing flow, turbulence, complete fluidization, or simple shear throughout the vertical profile are not appropriate models. Very low friction at the base or in a thin basal layer is necessary to allow the very long runouts. A component of motion resistance comes from the brittle plug of the slide, which spreads by bulk pure shear and faulting only so long as the driving forces are greater than the resistance.

The experiments and natural examples show that our structural approach can provide much needed information on rockslide-avalanche kinematics. To model the emplacement of a rockslide avalanche, such structural work is a crucial first step in determining the conditions of emplacement. For predicting runouts and paths, the topography and potential source material must be characterized, and such data can be used for input into any physical model of emplacement.

ACKNOWLEDGMENTS

We thank Tim Druitt, Valentin Troll, Tim Davies, and Frances Garland for discussion and comments. We also thank two anonymous reviewers for their careful examination, as well as Thomas Walter and Clause Siebe for their useful corrections.

REFERENCES CITED

Belousov, A., Belousova, M., and Voight, B., 1999, Multiple edifice failures, debris avalanches and associated eruptions in the Holocene history of Shiveluch volcano, Kamchatka, Russia: Bulletin of Volcanology, v. 61, p. 324–342, doi: 10.1007/s004450050300.

Bernard, B., van Wyk de Vries, B., Barba, D., Robin, C., Léyrit, H., Alcaraz, S., and Samaniego, P., 2008, The Chimborazo sector collapse and debris avalanche: Deposit characteristics as evidence of emplacement mechanisms: Journal of Volcanology and Geothermal Research (in press).

Borgia, A., and van Wyk de Vries, B., 2003, The volcano-tectonic evolution of Concepcion, Nicaragua: Bulletin of Volcanology, v. 65, p. 248–266.

Campbell, C.S., 1989, Self-lubrication for long runout landslides: Journal of Geology, v. 97, p. 653–665.

Campbell, C.S., Cleary, P.W., and Hopkins, M.J., 1995, Large-scale landslide simulations: Global deformation, velocities and basal friction: Journal of Geophysical Research, v. 100, p. 8267–8283, doi: 10.1029/94JB00937.

Cecchi, E., van Wyk de Vries, B., and Lavest, J.M., 2004, Flank spreading and collapse of weak-cored volcanoes: Bulletin of Volcanology, v. 67, p. 72–91, doi: 10.1007/s00445-004-0369-3.

Clavero, J.E., Sparks, R.S.J., and Huppert, H.E., 2002, Geological constraints on the emplacement mechanism of the Parinacota avalanche, northern Chile: Bulletin of Volcanology, v. 64, p. 40–54, doi: 10.1007/s00445-001-0183-0.

Clavero, J.E., Polanco, E., Godoy, E., Aguilar, G., Sparks, S., van Wyk de Vries, B., Pérez de Arce, C., and Matthews, S., 2005, Substrata influence in the transport and emplacement mechanisms of the Ollagüe debris avalanche, northern Chile: Acta Vulcanologica v. 16, p. 31–48.

Crandell, D.R., 1989, Gigantic debris avalanche of Pleistocene age from ancestral Mount Shasta Volcano, California, and debris-avalanche hazard zonation: U.S. Geological Survey Bulletin 1861, 32 p.

Cruden, D.M., and Varnes, D.J., 1996, Landslide types and processes, *in* Turner A.K., and Shuster, R.L., eds., Landslides: Investigation and mitigation: Transportation Research Board and National Research Council Special Report 247, p. 36–75.

Dade, W.B., and Huppert, H.E., 1998, Long-runout rockfalls: Geology, v. 26, p. 803–806, doi: 10.1130/0091-7613(1998)026<0803:LRR>2.3.CO;2.

Davies, T.R.H., McSaveney, M.J., and Hodgson, K.A., 1999, A fragmentation-spreading model for long runout rock avalanches: Canadian Geotechnical Journal, v. 36, p. 1096–1110, doi: 10.1139/cgj-36-6-1096.

Denlinger, R.P., and Iverson, R.M., 2001, Flow of variably fluidized granular masses across three-dimensional terrain 2, Numerical predictions and experimental tests: Journal of Geophysical Research, v. 106, no. B1, p. 553–566, doi: 10.1029/2000JB900330.

Donnadieu, F., 2000, Destabilization of volcanic edifices by cryptodomes: Analog modeling and numerical approach [Ph.D. thesis]: Université Blaise Pascal, Clermont-Ferrand II, 256 p.

Donnadieu, F., and Merle, O., 1998, Experiments on the indentation process during cryptodome intrusions: New insights into Mount St. Helens deformation: Geology, v. 26, p. 79–82, doi: 10.1130/0091-7613(1998)026<0079:EOTIPD>2.3.CO;2.

[3]If you are viewing the PDF of this paper or reading it offline, please visit http://dx.doi.org/10.1130/GES00131.S2 (Table S2) or the full-text article on www.gsajournals.org to view Supplemental Table S2.

Duran, J., 1997, Sables, Poudres et Grains: Paris, Eyrolles, 251 p.

Eppler, D.B., Fink, J., and Fletcher, R., 1987, Rheologic properties and kinematics of emplacement of the Chaos Jumbles rockfall avalanche, Lassen Volcanic National Park, California: Journal of Geophysical Research, v. 92, p. 3623–3633, doi: 10.1029/JB092iB05p03623.

Francis, P.W., and Wells, G.L., 1988, Landsat Thematic Mapper observations of debris avalanche deposits in the Central Andes: Bulletin of Volcanology, v. 50, p. 258–278, doi: 10.1007/BF01047488.

Francis, P.W., Gardeweg, M., O'Callaghan, L.J., Ramirez, C.F., and Rothery, D.A., 1985, Catastrophic debris avalanche deposit of Socompa volcano, north Chile: Geology, v. 13, p. 600–603, doi: 10.1130/0091-7613(1985)13<600:CDADOS>2.0.CO;2.

Glicken, H., 1991, Sedimentary architecture of large volcanic-debris avalanches, *in* Fisher R.V., and Smith G.A., eds., Sedimentation in volcanic settings: SEPM (Society for Sedimentary Geology) Special Publication 45, p. 99–106.

Glicken, H., 1998, Rockslide-debris avalanche of May 18, 1980, Mount St. Helens Volcano, Washington: Geological Society of Japan Bulletin, v. 49, no. 2/3, p. 55–106.

Glicken, H., Voight, B., and Janda, R.J., 1981, Rockslide-debris avalanche of May 18, 1980, Mount St. Helens volcano: IAVCEI Symposium on Arc Volcanism, Tokyo and Hakone: Tokyo, Terra Scientific Publishing Co., p. 109–110.

Gray, J.M.N.T., and Thorton, A.R., 2005, A theory for particle size segregation in shallow granular free-surface flows: Royal Society of London Proceedings, ser. A, v. 461, no. 2056, p. 1447–1473.

Guilbaud, M.N., 2000, Structural analysis of the emplacement of the Socompa debris avalanche [M.S. thesis]: Université Blaise Pascal, Clermont-Ferrand, France.

Heim, A., 1932, Bergsturz und Menchenleben: Zurich, Vierteljahrsschrift, v. 77, no. 20, 218 p.

Hornbaker, D.J., Albert, R., Albert, I., Barabasi, A.L., and Schiffer, P., 1997, What keeps sandcastles standing: Nature, v. 387, p. 765, doi: 10.1038/42831.

Howard, K., 1973, Avalanche mode of motion: Implications from lunar examples: Science, v. 180, p. 1052–1055, doi: 10.1126/science.180.4090.1052.

Hungr, O., and Evans, S.G., 2004, Entrainment of debris in rock avalanches: An analysis of a long runout mechanism: Geological Society of America Bulletin, v. 116, p. 1240–1252, doi: 10.1130/B25362.1.

Iverson, R.M., and Denlinger, R.P., 2001, Flow of variably fluidized granular masses across three-dimensional terrain 1, Coulomb mixture theory: Journal of Geophysical Research, v. 106, no. B1, p. 537–552, doi: 10.1029/2000JB900329.

Kelfoun, K., and Druitt, T.H., 2005, Numerical modelling of the emplacement of Socompa rock avalanche, Chile: Journal of Geophysical Research, v. 110, no. B12, B12202, doi: 10.1029/2005JB003758.

Kelfoun, K., Druitt, T.H., van Wyk de Vries, B., and Guilbaud, M-N., 2008, The topographic reflection of the Socompa debris avalanche: Bulletin of Volcanology (in press).

Kilburn, C., and Sørensen, S.-A., 1998, Runout lengths of sturzstroms: The control of initial conditions and of fragment dynamics: Journal of Geophysical Research, v. 103, no. B8, p. 17,877–17,884, doi: 10.1029/98JB01074.

Lagmay, A.M.F., van Wyk de Vries, B., Kerle, N., and Pyle, D.M., 2000, Volcano instability induced by strike-slip faulting: Bulletin of Volcanology, v. 62, p. 331–346, doi: 10.1007/s004450000103.

Legros, F., 2002, The mobility of long-runout landslides: Engineering Geology, v. 63, p. 301–331, doi: 10.1016/S0013-7952(01)00090-4.

Lucchitta, B.K., 1979, Landslides in Valles Marineris, Mars: Journal of Geophysical Research, v. 84, p. 8097–8113, doi: 10.1029/JB084iB14p08097.

McEwen, A., 1989, Mobility of large rock avalanches: Evidence from Valles Marineris, Mars: Geology, v. 17, p. 1111–1114, doi: 10.1130/0091-7613(1989)017<1111:MOLRAE>2.3.CO;2.

Merle, O., and Borgia, A., 1996, Scaled experiments of volcanic spreading: Journal of Geophysical Research, v. 101, p. 13,805–13,817, doi: 10.1029/95JB03736.

Merle, O., and Donnadieu, F., 2000, Indentation of volcanic edifices by the ascending magma, *in* Vendeville, B., et al., eds., Salt, shale and igneous diapirs in and around Europe: Geological Society of London Special Publication 174, p. 43–53.

Merle, O., Vidal, N., and van Wyk de Vries, B., 2001, Experiments on vertical basement fault reactivation below volcanoes: Journal of Geophysical Research, v. 106, no. B2, p. 2153–2162, doi: 10.1029/2000JB900352.

Middleton, G.V., and Wilcock, P.R., 1994, Mechanics in the Earth and environmental sciences: Cambridge, Cambridge University Press, 455 p.

Oehler, J.F., Labazuy, P., and Lenat, J.F., 2004, Recurrence of major flank landslides during the last 2-Ma-history of Reunion Island: Bulletin of Volcanology, v. 66, p. 585–598, doi: 10.1007/s00445-004-0341-2.

Oehler, J.F., van Wyk de Vries, B., and Labazuy, P., 2005, Landslides and spreading of oceanic hot-spot and arc shield volcanoes on Low Strength Layers (LSLs): An analogue modelling approach: Journal of Volcanology and Geothermal Research, v. 144, p. 169–189, doi: 10.1016/j.jvolgeores.2004.11.023.

Pollet, N., and Schneider, J.-L., 2004, Dynamic disintegration processes accompanying transport of the Holocene Flims sturzström (Swiss Alps): Earth and Planetary Science Letters, v. 221, p. 433–448, doi: 10.1016/S0012-821X(04)00071-8.

Pouliquen, O., and Renaut, N., 1996, Onset of granular flows on an inclined rough surface: Dilatancy effects: Journal de Physique II, v. 6, p. 923–935, doi: 10.1051/jp2:1996220.

Pudasaini, S.P., and Hutter, K., 2007, Avalanche dynamics: Dynamics of rapid flows of dense granular avalanches: Netherlands, Springer, 602 p.

Ramberg, H., 1981, Gravity, deformation and the Earth's crust in theory, experiments and geological applications (second edition): London, Academic Press, 452 p.

Reiche, P., 1937, The Toreva-block, a distinctive landslide type: Journal of Geology, v. 45, p. 538–548.

Reubi, O., and Hernández, J., 2000, Volcanic debris avalanche of the upper Maronne valley (Cantal Volcano, France): Evidence for contrasted formation and transport mechanisms: Journal of Volcanology and Geothermal Research, v. 102, p. 271–286, doi: 10.1016/S0377-0273(00)00191-8.

Savage, S.B., and Lun, C.K.K., 1988, Particle size segregation in inclined chute flow of dry cohesionless granular solids: Journal of Fluid Mechanics, v. 189, p. 311–335, doi: 10.1017/S002211208800103X.

Scheidegger, A.E., 1973, On the prediction of the reach and velocity of catastrophic landslides: Rock Mechanics, v. 5, p. 231–236, doi: 10.1007/BF01301796.

Schenk, P.M., and Bulmer, M.H., 1998, Origin of mountains on Io by thrust faulting and large-scale mass movements: Science, v. 279, p. 1514–1517, doi: 10.1126/science.279.5356.1514.

Shaller, P.J., 1991, Analysis and implications of large Martian and terrestrial landslides [Ph.D. thesis]: Pasadena, California Institute of Technology, 586 p.

Shea, T., van Wyk de Vries, B., and Pilato, M., 2007, Emplacement mechanisms of contrasting debris avalanches at Volcán Mombacho (Nicaragua), provided by structural and facies analysis: Bulletin of Volcanology, doi: 10.1007/s00445–007–0177–7.

Shreve, R.L., 1966, Sherman landslide, Alaska: Science, v. 154, p. 1639–1643, doi: 10.1126/science.154.3757.1639.

Shreve, R.L., 1968, The Blackhawk landslide: Geological Society of America Special Paper 108, p. 1–47.

Siebe, C., Komorowski, J.-C., and Sheridan, M.F., 1992, Morphology and emplacement of an unusual debris-avalanche deposit at Jocotitlán volcano, central Mexico: Bulletin of Volcanology, v. 54, p. 573–589, doi: 10.1007/BF00569941.

Siebert, L., 1984, Large volcanic debris avalanches: Characteristics of source areas, deposits, and associated eruptions: Journal of Volcanology and Geothermal Research, v. 22, p. 163–197, doi: 10.1016/0377-0273(84)90002-7.

Siebert, L., Glicken, H., and Ui, T., 1987, Volcanic hazards from Bezymianny- and Bandaï-type eruptions: Bulletin of Volcanology, v. 49, p. 435–459, doi: 10.1007/BF01046635.

Siebert, L., Alvarado, G., Vallance, J.W., and van Wyk de Vries, B., 2006, Large-volume volcanic edifice failures in Central America and associated hazards, *in* Rose, W.I., et al., eds., Volcanic hazards in Central America: Geological Society of America Special Paper 412, p. 1–26, doi: 10.1130/2006.2412(01).

Staron, L., Vilotte, J.P., and Radjai, F., 2001, Friction and mobilization of contacts in granular numerical avalanches, *in* Kishino, Y., ed., Powders and grains: Lisse, Netherlands, Swets and Zeitlinger, p. 451–454.

Stoopes, G.R., and Sheridan, M.F., 1992, Giant debris avalanches from the Colima volcanic complex, Mexico: Implication for long-runout landslides (100 km) and hazard assessment: Geology, v. 20, p. 299–302, doi: 10.1130/0091-7613(1992)020<0299:GDAFTC>2.3.CO;2.

Ui, T., 1983, Volcanic dry avalanche deposits: Identification and comparison with non-volcanic debris stream deposits: Journal of Volcanology and Geothermal Research, v. 18, p. 135–150, doi: 10.1016/0377-0273(83)90006-9.

van Wyk de Vries, B., and Borgia, A., 1996, The role of basement in volcano deformation, *in* McGuire, W.J., et al., eds., Volcano instability on the Earth and other planets: Geological Society of London Special Publication 110, p. 95–110.

van Wyk de Vries, B., and Francis, P.W., 1997, Catastrophic collapse at stratovolcanoes induced by gradual volcano spreading: Nature, v. 387, p. 387–390.

van Wyk de Vries B., and Merle, O., 1996, The effect of volcanic constructs on rift fault patterns: Geology, v. 24, p. 643–646, doi: 10.1130/0091-7613(1996)024<0643:TEOVCO>2.3.CO;2.

van Wyk de Vries, B., Self, S., Francis, P.W., and Keszthelyi, L., 2001, A gravitational spreading origin for the Socompa debris avalanche: Journal of Volcanology and Geothermal Research, v. 105, p. 225–247, doi: 10.1016/S0377-0273(00)00252-3.

van Wyk de Vries, B., Gilbaud, M-N., Self, S., and Druitt, T., 2002, A brittle crust during the emplacement of the Socompa debris avalanche?: Nice, European Geosciences Union general assembly, 1st, abs. EGU04-A-02057.

Voight, B., 1981, Time scale for the first moments of the May 18 eruption, *in* Lipman, P.W., and Mullineaux, D.R., eds., The 1980 eruptions of Mount St. Helens, Washington: U.S. Geological Survey Professional Paper 1250, p. 69–86.

Voight, B., Glicken, H., Janda, R.J., and Douglass, P.M., 1981, Catastrophic rockslide avalanche of May 18, *in* Lipman, P.W., and Mullineaux, D.R., eds., The 1980 eruptions of Mount St. Helens, Washington: U.S. Geological Survey Professional Paper 1250, p. 347–377.

Voight, B., Janda, R.J., Glicken, H., and Douglass, P.M., 1983, Nature and mechanics of the Mount St. Helens rockslide avalanche of 18 May 1980: Geotechnique, v. 33, p. 243–273.

Wadge, G., Francis, P.W., and Ramirez, C.F., 1995, The Socompa collapse and avalanche event: Journal of Volcanology and Geothermal Research, v. 66, p. 309–336, doi: 10.1016/0377-0273(94)00083-S.

Manuscript Received 24 May 2007
Revised Manuscript Received 06 April 2008
Manuscript Accepted 29 April 2008